Title

Room-temperature structural studies of SARS-CoV-2 protein NendoU with an X-ray free-electron laser.

Journal

Structure (London, England : 1993), 31(2)

ISSN

0969-2126

Authors

Jernigan, Rebecca J
Logeswaran, Dhenugen
Doppler, Diandra
et al.

Publication Date

2023-02-01

DOI

10.1016/j.str.2022.12.009

Peer reviewed

Since January 2020 Elsevier has created a COVID-19 resource centre with free information in English and Mandarin on the novel coronavirus COVID-19. The COVID-19 resource centre is hosted on Elsevier Connect, the company's public news and information website.

Structure

Article

Room-temperature structural studies of SARS-CoV-2 protein NendoU with an X-ray free-electron laser

Graphical abstract

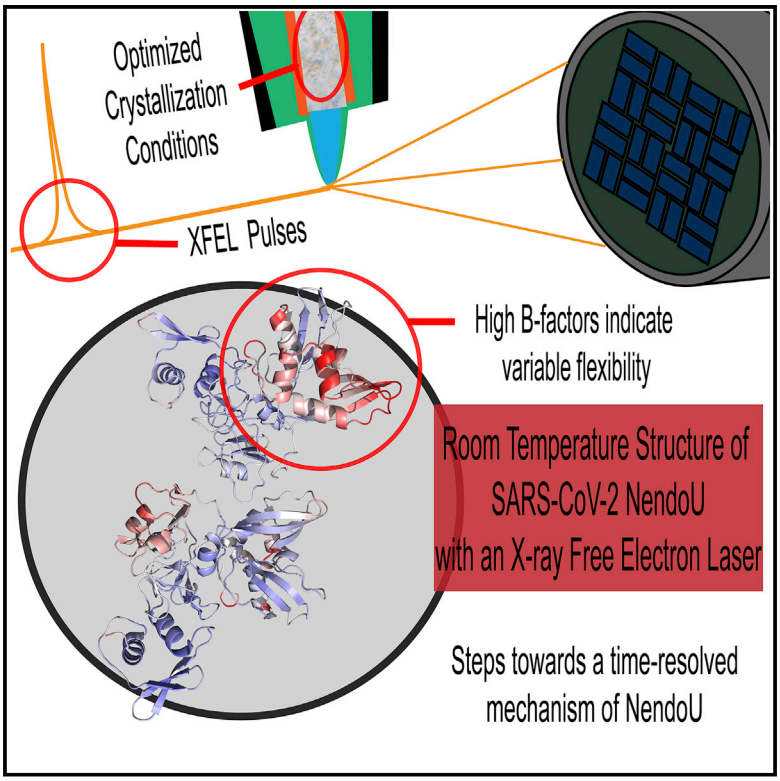

Highlights

- The first room-temperature structure of NendoU from SARS-CoV-2 is solved at an XFEL
- Designed RNA substrates are cleaved within microcrystals of NendoU
- High B factors indicate varying flexibility between trimers of the NendoU hexamer
- Alternating trimer flexibility suggests a binding-change mechanism

Authors

Rebecca J. Jernigan, Dhenugen Logeswaran, Diandra Doppler, ..., Julian J.-L. Chen, Sabine Botha, Petra Fromme

Correspondence

sbotha@asu.edu (S.B.), pfromme@asu.edu (P.F.)

In brief

NendoU from SARS-CoV-2 is a protein responsible for the virus's ability to evade the immune system. Jernigan et al. report the room-temperature structure of NendoU, finding indications that it functions by an alternate-switch mechanism. This sets a benchmark for studies targeting this enzyme in treating coronavirus infections.

Jernigan et al., 2023, Structure *31*, 138–151
February 2, 2023
https://doi.org/10.1016/j.str.2022.12.009

CellPress

CellPress

Structure

Article

Room-temperature structural studies of SARS-CoV-2 protein NendoU with an X-ray free-electron laser

Rebecca J. Jernigan,[1,2] Dhenugen Logeswaran,[2] Diandra Doppler,[1,2] Nirupa Nagaratnam,[1] Mukul Sonker,[1,2] Jay-How Yang,[1] Gihan Ketawala,[1,2] Jose M. Martin-Garcia,[1,10] Megan L. Shelby,[3] Thomas D. Grant,[4] Valerio Mariani,[5] Alexandra Tolstikova,[6] Michelle Z. Sheikh,[1] Mimi Cho Yung,[3] Matthew A. Coleman,[3] Sahba Zaare,[1,7,8] Emily K. Kaschner,[1,2] Mohammad Towshif Rabbani,[1] Reza Nazari,[1] Michele A. Zacks,[1] Brandon Hayes,[5] Raymond G. Sierra,[5] Mark S. Hunter,[5] Stella Lisova,[5] Alexander Batyuk,[5] Christopher Kupitz,[5] Sebastien Boutet,[5] Debra T. Hansen,[1] Richard A. Kirian,[1,8] Marius Schmidt,[9] Raimund Fromme,[1,2] Matthias Frank,[3] Alexandra Ros,[1,2] Julian J.-L. Chen,[2] Sabine Botha,[1,8,*] and Petra Fromme[1,2,11,*]

[1]Biodesign Center for Applied Structural Discovery, Arizona State University, Tempe, AZ 85287-5001, USA
[2]School of Molecular Sciences, Arizona State University, Tempe, AZ 85287-1604, USA
[3]Lawrence Livermore National Laboratory, 7000 East Avenue, Livermore, CA 94550, USA
[4]Department of Structural Biology, Jacobs School of Medicine and Biomedical Sciences, SUNY University at Buffalo, 955 Main Street, Buffalo, NY 14203, USA
[5]Linac Coherent Light Source, SLAC National Accelerator Laboratory, Menlo Park, CA 94025, USA
[6]Deutsches Elektronen-Synchrotron, Notkestrasse 85, 22607 Hamburg, Germany
[7]Fulton School of Electrical, Computer, and Energy Engineering, Arizona State University, Tempe, AZ 85287, USA
[8]Department of Physics, Arizona State University, Tempe, AZ 85287-1504, USA
[9]Department of Physics, University of Wisconsin-Milwaukee, 3135 N. Maryland Avenue, Milwaukee, WI 53211, USA
[10]Present address: Department of Crystallography and Structural Biology, Institute of Physical Chemistry "Rocasolano," CSIC, Serrano 119, 28006, Madrid, Spain
[11]Lead contact
*Correspondence: sbotha@asu.edu (S.B.), pfromme@asu.edu (P.F.)
https://doi.org/10.1016/j.str.2022.12.009

SUMMARY

NendoU from SARS-CoV-2 is responsible for the virus's ability to evade the innate immune system by cleaving the polyuridine leader sequence of antisense viral RNA. Here we report the room-temperature structure of NendoU, solved by serial femtosecond crystallography at an X-ray free-electron laser to 2.6 Å resolution. The room-temperature structure provides insight into the flexibility, dynamics, and other intrinsic properties of NendoU, with indications that the enzyme functions as an allosteric switch. Functional studies examining cleavage specificity in solution and in crystals support the uridine-purine cleavage preference, and we demonstrate that enzyme activity is fully maintained in crystal form. Optimizing the purification of NendoU and identifying suitable crystallization conditions set the benchmark for future time-resolved serial femtosecond crystallography studies. This could advance the design of antivirals with higher efficacy in treating coronaviral infections, since drugs that block allosteric conformational changes are less prone to drug resistance.

INTRODUCTION

The uridine-specific nidoviral endoribonuclease (NendoU) protein (also known as nonstructural protein 15 [Nsp15]) from SARS-CoV-2 is highly conserved among coronaviruses and a potential target for drug discovery due to its role in viral evasion of the innate host immune system.[1] *In vitro* studies in mouse hepatitis virus show that loss of NendoU activity stimulates a protective immune response, which can be attributed to an increase in double-stranded RNA (dsRNA).[2] Mouse model studies further showed that NendoU is essential for virus replication with minimal response by macrophages and natural killer cells, and inactivating NendoU results in a greatly attenuated disease progression.[3] In the avian coronavirus infectious bronchitis virus (IBV), NendoU interferes with the formation of cytoplasmic stress granules and dsRNA accumulation, activities that have been demonstrated to mitigate the host antiviral response.[4]

The substrate of NendoU was identified as the 5′-polyuridine (poly[U]) leader sequence of (−) sense genomic RNA,[1] a pathogen-associated molecular pattern whereby dsRNA from replication intermediates of single-stranded RNA viruses stimulates the type 1 interferon response.[5] NendoU exhibits broad-spectrum cleavage, with cleavage preference apparent only for a purine 5′ of the cleavage site and being site specific only for

the uridine.[6] The first crystal structure of NendoU from SARS-CoV-2 was determined by Kim et al. and shows that it assembles into a hexamer formed by a dimer of homotrimers with a molecular weight (MW) of 39 kDa for the monomer.[7] The hexamer has been identified as critical for activity in SARS-CoV and SARS-CoV-2.[7–9] High conservation of sequence and structural identity between SARS-CoV-1, MERS-CoV, and SARS-CoV-2 makes NendoU an ideal drug target.[7] The catalytic center is located in the C-terminal domain and contains the conserved residues H235, H250, K290, S294, Y343, and L346. In earlier studies it was hypothesized that the dual histidine residues may cleave substrates via a mechanism similar to that of RNase A.[7,10,11] The precise function and cleavage mechanism of NendoU are still to be determined, but some recent studies suggest they are likely to be much more complex than those initially proposed. Specifically, a very different functional hypothesis places NendoU at the center of the replication-transcription complex, in which the dsRNA moves through the active site prior to separation into single-stranded RNA (ssRNA).[12] Supporting this hypothesis, NendoU was shown to cleave dsRNA in addition to ssRNA and cryoelectron microscopy (cryo-EM) analysis showed NendoU in complex with a 52 nt dsRNA.[13]

The ability to express and purify copious quantities of catalytically active recombinant NendoU has facilitated not only its structural characterization, but also the *in vitro* probing of its enzymatic function. A classical but powerful method is to incubate radiolabeled substrate RNA with NendoU, followed by resolution of the RNA cleavage products via polyacrylamide gel electrophoresis (PAGE). The cleavage pattern visualized by autoradiography provides the enzymatic cleavage specificities. This was first developed for the SARS-CoV-1 NendoU,[8,14,15] and a subsequent assay platform using fluorescently labeled RNA substrates has allowed scientists to overcome the disadvantages associated with handling radioactive material. This has been instrumental in the ability to conduct SARS-CoV-2 NendoU enzymatic studies.[6,16,17] Furthermore, a real-time enzymatic reaction monitoring assay based on Förster resonance energy transfer (FRET) has been used for studying NendoU enzyme activity and kinetics.[7,18] Due to the adaptability of this assay for monitoring hundreds of thousands of reactions simultaneously, it has been employed in high-throughput screening studies to identify small-molecule inhibitors of NendoU.[19,20] While both the gel-based and the FRET-based assays provide a wealth of information on RNA cleavage specificities and enzyme kinetics, respectively, they provide only indirect information on the underlying enzymatic mechanism. Mass spectrometric analysis has been used for determining the chemical nature of NendoU cleavage products, providing some insight into the catalytic mechanism.[18,21]

Structural information on NendoU is essential for fully understanding the enzymatic process, but the aforementioned cryo-EM and standard crystallography techniques are conducted under nonphysiological, cryogenic conditions. In contrast, time-resolved studies by serial femtosecond X-ray crystallography (TR-SFX) at X-ray free-electron lasers (XFELs) have been used successfully to study enzyme-catalyzed reactions at atomic resolution.[22–24] In SFX studies, thousands of single-crystal diffraction snapshots are collected from nano- and microcrystals as small as 100 nm at room temperature, which interact with the ultrashort, ultrabright X-ray pulses with 10–40 fs pulse duration of the XFEL. The pulse intensity is so strong that it destroys any solid material; however, the pulses are short enough that X-ray diffraction images are collected prior to the onset of secondary X-ray radiation damage.[25] This allows for structure determination of macromolecules at ambient temperature[25,26] using radiation doses well beyond the generally allowable Henderson limit. Biological reactions can be triggered "on the fly"[27] to study the mechanism of proteins through the use of a mix-and-inject technology.[22,28,29] This technology has been used to study the enzymatic function of β-lactamase C (BlaC) from *Mycobacterium tuberculosis*[22–24,28] and enabled dynamic studies of an RNA riboswitch.[30]

In the study described here, we report the structure of NendoU at room temperature at an XFEL. The data show differences in the flexibility of the two trimers in the hexamer, which has significant implications for the catalytic function of NendoU. In preparation for future TR-SFX studies, RNA substrates of varying lengths were designed based on analysis of the NendoU protein structure and genomic analysis of the SARS-CoV-2 RNA.

RESULTS

In vivo and cell-free recombinant expression to mitigate NendoU-mediated *E. coli* cytotoxicity

For XFEL studies, large protein quantities are required. This was a challenge for the SFX NendoU project, since the expression yields were very low. Using the published expression protocol for NendoU from Kim et al.,[7] 1–3 mg of NendoU protein was isolated per liter of cell culture. For optimization of the expression conditions, varying the cell culture medium, temperature, and time of induction was tested. However, no significant improvement in the protein yield was achieved. NendoU toxicity to the expressing host cell and low expression yield have been previously reported.[31] Fresh weekly transformation was essential to prevent reduced expression yield. To isolate 300 mg of wild-type NendoU for the RT-SFX experiments, we scaled up expression and isolation to grow and purify over 300 L of liquid culture. NendoU was isolated from the cytosol by metal-affinity chromatography (Figure S1A) followed by size-exclusion chromatography (SEC), and the purified protein (hexamer) was verified by SDS-PAGE with Coomassie stain and western blot (Figures S1B–S1F). Dynamic light-scattering experiments showed that the hexameric protein was monodisperse and suitable for crystallization experiments (Figure S1E).

The potential toxicity effects on the *in vivo* expression of NendoU were addressed by implementing an *in vitro E. coli*-based cell-free expression platform. Initial small-scale expression screening with varied pHis-TEV-Nsp15 plasmid concentrations utilized reaction mixtures including a tRNA that incorporates BODIPY-labeled lysine into *in vitro* translation products. After expression, the reaction mixtures containing the whole lysate were analyzed via SDS-PAGE and imaged at 600 nm to visualize the incorporated BODIPY, which clearly detected a 41 kDa translation product that corresponded to NendoU in all reactions containing the pHis-TEV-Nsp15 plasmid (Figure 1A). Higher-molecular-weight contaminants were not apparent in this analysis.

Scale-up reactions of 1 mL volume were performed to assess the translation products. Reaction products were purified from the cell-free lysate as described in the STAR Methods and

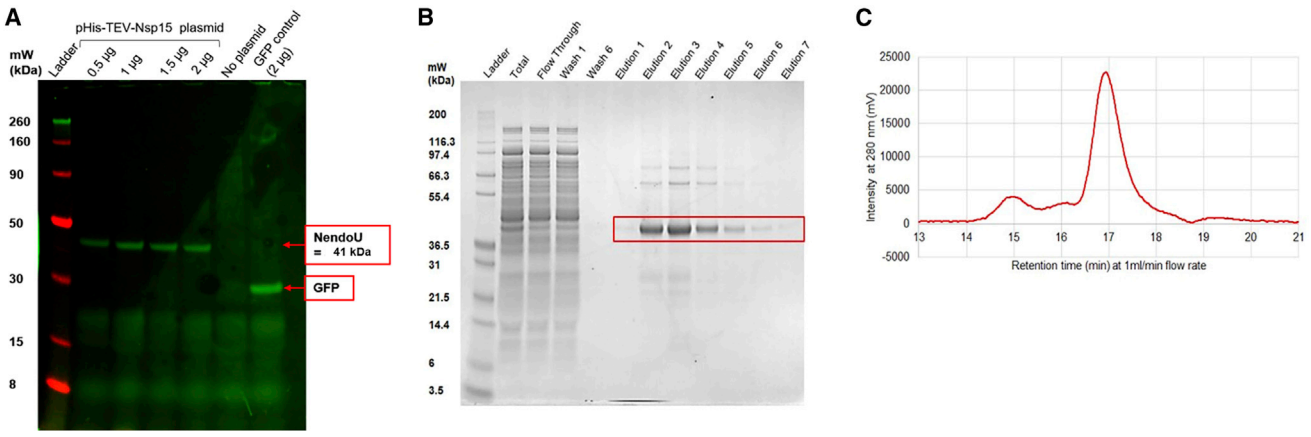

Figure 1. *In vitro* cell-free expression of NendoU

(A) BODIPY-labeled cell-free expression products from expression screening of pHis-TEV-Nsp15 plasmid. A 4%–12% Bis-Tris SDS-PAGE gel imaged at 700 (red) and 600 nm (green) to visualize the Li-cor Chameleon 700 nm ladder is shown.

(B) Fractions from gravity-flow Ni-NTA purification of 1 mL of preparative cell-free expression of NendoU assayed with SDS-PAGE. Samples were run on a 4%–12% Bis-Tris SDS-PAGE gel, stained with SYPRO orange, and imaged at 600 nm.

(C) SEC chromatogram for pooled and concentrated elution fractions from Ni-NTA purification of 1 mL of preparative cell-free expression of NendoU. The protein was purified with a Superdex 200 in 20 mM HEPES-Na (pH 7.5), 150 mM NaCl, and 1 mM TCEP at 1 mg/mL. A representative chromatogram from a 50 µg test injection is shown.

analyzed by SDS-PAGE (Figure 1B). The elution fractions showed a strong band at 39 kDa with some minimal contaminant bands present at approximately 60 and 75 kDa. Protein quantification of the elution fractions leads to NendoU yields of 0.8 mg/mL. Further purification with SEC results in an elution profile very similar to those produced during the purification of NendoU expressed *in vivo* (Figures 1C and S1C).

Designing the optimal RNA substrate

To determine whether the cleavage of the natural poly(U) leader sequence by NendoU is structure or sequence dependent, a systematic approach was used to design an optimal RNA substrate. Multiple sequence alignment of the native cleavage site, downstream sequences of SARS-CoV-2, and closely related coronavirus negative-strand RNAs was performed (Figure 2A). While the first nucleotide following the poly(U) tract was an invariant G residue (Figure 2A, black highlighted sequence), the alignment revealed a conserved 4 bp stem (Figure 2B) supported by co-variation immediately downstream of this G nucleotide. Previous RNA secondary structure modeling studies using the sequence of SARS-CoV-2's negative-strand 3′ UTR did not predict this hairpin, which is likely due to the reduced focus on evolutionary conservation in the prediction method used.[32] Hence, to determine whether the length of the poly(U) tract or the presence of the conserved 4 bp hairpin influences the cleavage activity or specificity of NendoU, we designed five different substrates that were labeled with a near-infrared 800 nm (NIR-800) fluorophore on the 3′ end (Figure 2C). Substrates 1 and 2 have 3 and 6 U residues, respectively. Substrate 3 has a mutated U nucleotide in the loop region, and substrates 4 and 5 harbor mutations either disrupting or reinforcing the base pairing of the 4 bp stem.

Endoribonuclease assays were set up with 0.6 µM NendoU and 0.5 µM respective NIR-800-labeled RNA in the presence of 5 mM $MnCl_2$ (Figure 2D), including a control without NendoU. Both RNA substrates 1 and 2 are predominantly cleaved 3′ of the last U residue of the 5′ U tract with similar efficiencies regardless of the length of the U leader, suggesting that the length of the U tract does not play a significant role in NendoU cleavage efficiency. RNA substrate 4 was predominantly cleaved 3′ of the analogous loop U nucleotide (eighth U from the 5′ end).

However, the four U residues upstream of this U and downstream of the first U-G junction in substrate 4 do not seem to be preferred. First, it may be that the analogous loop U residue is cleaved with higher efficiency in substrate 4 than in substrate 1 or 2 due to the destabilization of the 4 bp stem, which may facilitate better access of NendoU to this residue; substrates 1 and 2 have a stable stem that might restrict binding of the loop U residue to the NendoU active site (Figure 2C). Second, mutating the loop U residue to a C in substrate 3 completely abolishes cleavage of the bond following this nucleotide (Figure 2D), consistent with a pattern in which cleavage occurs 3′ of a U residue. Finally, substrate 5 is cleaved only after the third U and not the fifth, reinforcing the idea that a G or an A is needed 3′ of the U for efficient cleavage. Overall, these data suggest that the preferred bond cleaved by NendoU is between a U and a purine, with cleavage occurring 3′ of the U. The preferred substrate is unstructured RNA, as structural elements involving the cleavage site or proximal to the cleavage site have lower cleavage efficiency. Thus, substrate 5, which has a single preferred cleavage site with a stable stem, is suitable for crystallographic purposes and was selected for downstream experiments.

Next, we aimed to determine the minimal length of the substrate capable of being cleaved by NendoU. In preparation, we measured the length of the active-site cleft using the previously published structure of SARS-CoV-2 NendoU (PDB: 6VWW), which was estimated to be ~19.3 Å (Figure 2E). A 6 nt and a

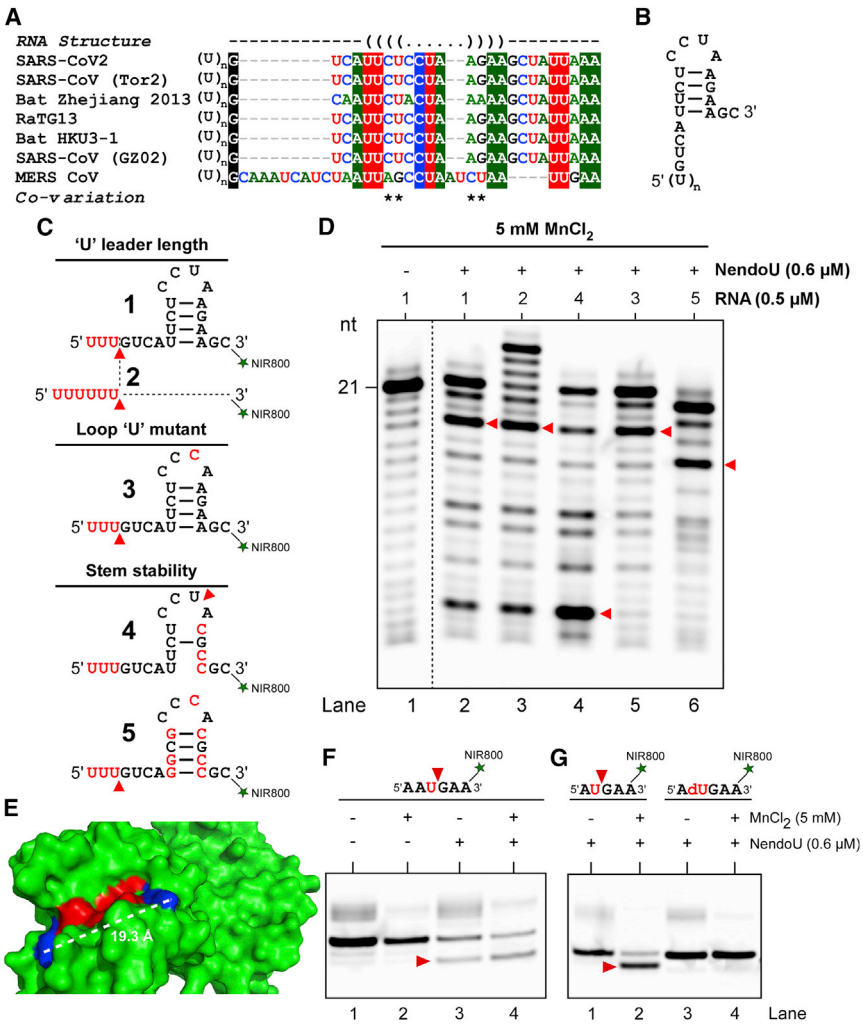

Figure 2. Design of RNA substrates for NendoU cleavage that mimic the 5′ end of the SARS-CoV-2 antisense RNA

SARS-CoV-2 NendoU cleavage specificity and the optimal substrate were determined for TR-SFX.

(A) Multiple sequence alignment of nucleotides immediately downstream of the poly(U) leader sequence of negative-strand RNA of SARS-CoV-2 and related coronaviruses. Nucleotides are colored in red (U), blue (C), green (A), and black (G). Nucleotides showing 100% conservation are highlighted with white text on colored background. RNA structure is shown as dot-bracket notation above the alignment with co-varying residues marked with an asterisk underneath the alignment.

(B) Secondary structure model of the first 21 nt of SARS-CoV-2 negative-strand RNA immediately downstream of the poly(U) leader sequence, determined based on the multiple sequence alignment shown in (A).

(C) Secondary structure models of synthetic RNA oligos to test the effects of various sequence or structural properties on NendoU activity. Expected major cleavage sites are shown with red arrowheads.

(D) NendoU endoribonuclease assay gel for substrates in (C), with bands corresponding to major cleavage sites shown with red arrowheads.

(E) Surface representation of NendoU crystal structure (PDB: 6VWW) with the active-site cleft colored in red and putative RNA-interacting amino acids flanking the active site colored in blue. The distance between the blue residues is 19.3 Å as measured in PyMol (Schrödinger, Inc.), shown by a white dotted line.

(F) NendoU endoribonuclease assay for the 6 nt RNA substrate. RNA sequence is shown above the gel and the major cleavage site indicated both above the sequence and at the corresponding band in the gel.

(G) NendoU endoribonuclease assay for the cleavable and uncleavable 5 nt RNA substrate. Respective RNA sequences are shown above the gel and the major cleavage site is indicated both above the sequence and at the corresponding band in the gel for the cleavable substrate.

5 nt substrate were designed with a single preferred U-G cleavage site: 5′-AAUGAA-3′ and 5′-AUGAA-3′, respectively. Both substrates were cleaved with high efficiency by NendoU at the expected cleavage sites (Figure 2F), while controls without NendoU produced intact substrate bands. In addition, we had synthesized an identical 5 nt substrate with a 2′-deoxyuridine, which does not contain the 2′-hydroxyl on the uridine, which should prevent enzymatic cleavage. As expected, NendoU did not process this substrate (Figure 2G). Thus, the cleavable and the uncleavable 5 nt RNAs were the substrates of choice for further analysis. In summary, the functional assays using RNA substrates that are variants of NendoU's native cleavage sequence have shown that the 5 nt 5′-AUGAA-3′ oligonucleotide with a preferred UG cleavage site is a minimal substrate sufficient for NendoU catalysis to occur.

Microcrystallization of NendoU protein

Microcrystallization conditions for NendoU were established and optimized for the SFX experiments at the Linac Coherent Light Source (LCLS) at SLAC (Menlo Park, CA). Two different techniques were used to obtain crystals: crystallization by concentration and batch with agitation in the presence of sodium citrate (Figure 3). In crystallization by concentration, the overall solubility of the solution is decreased by concentrating the protein at low-salt concentration. During this process the surface of the protein molecules becomes depleted of counterions, thereby fostering formation of crystal contacts between protein side chains of opposite charge. This method has been used previously for crystallization of the large photosynthetic membrane protein photosystem I for SFX.[33] When NendoU protein is concentrated beyond 50 mg/mL at 4°C, crystals with a needle-like morphology can be observed. The size was estimated to be between 5 and 10 μm in their longest dimension.

In the second approach, NendoU crystals were grown by the batch crystallization method with agitation. A protein solution is added dropwise to the precipitant solution under agitation at room temperature. Figure 3B illustrates how the nucleation zone is reached stepwise in the phase diagram using this method. NendoU crystals grown in the batch-with-agitation

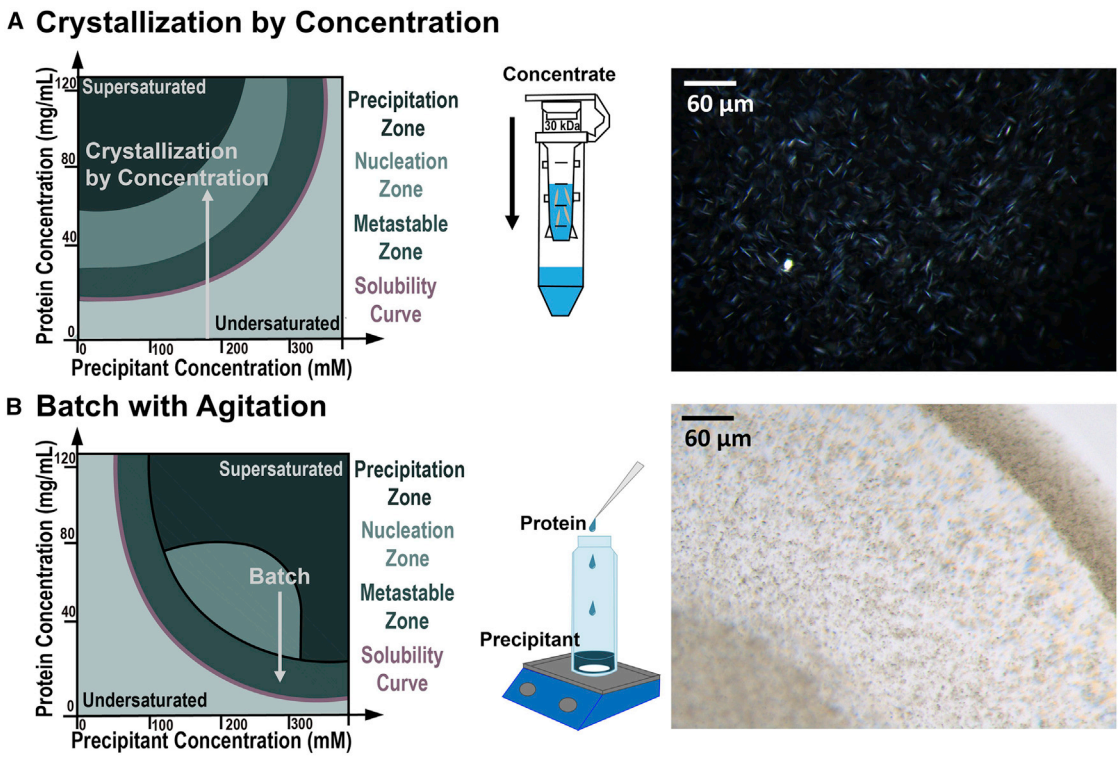

Figure 3. Microcrystallization of NendoU for SFX studies

(A) The crystallization by concentration method uses a high-protein concentration under low ionic strength. Within a protein concentration range of 60–80 mg/mL, the solution turns turbid. Crystals with a needle morphology, 5–10 μm in size, were observed.

(B) In batch with agitation, the protein is added dropwise to the precipitant in a glass vial with agitation. Crystals are grown in the presence of sodium citrate. This method produced 2 × 2 × 2 μm^3 crystals with a shard morphology.

method have a shard morphology and were approximately 2 × 2 × 2 μm^3 in size. Here, this crystallization approach is also referred to as the "citrate condition," in reference to the buffer component in the precipitant of this crystallization condition. Crystallization conditions were re-optimized at the conclusion of the SFX experiments to remove the citrate from the batch-with-agitation condition. Two conditions were identified using a standard batch method with different precipitant solutions, both generating 10–15 μm crystals with a rod morphology (Figure S2). These crystals were tested briefly at the LCLS at a protein crystal screening (PCS) beamtime (P182/185) in October 2020 and diffracted comparable to crystals grown from the citrate condition.

NendoU is fully active in microcrystals

To assess whether NendoU protein remains enzymatically active within crystals grown from the batch-with-agitation method, endoribonuclease assays were performed by incubating substrate 5 (Figure 2C) with crystals both in the presence and in the absence of Mn^{2+}. NendoU could efficiently cleave the RNA substrate even in the absence of Mn^{2+} ions (Figure 4A), suggesting that Mn^{2+} ions are not essential for in-crystal enzymatic cleavage. Additional experiments were performed to verify that the substrate cleavage by NendoU was due to protein present within the crystals as opposed to residual dissolved protein remaining in the supernatant. The crystals were pelleted by centrifugation following the reaction, and the supernatant was removed and replaced with fresh precipitant solution five times. The crystals were then pelleted one final time, the supernatant was removed, and RNA cleavage was assayed both in the presence and in the absence of Mn^{2+} (Figure 4B) with the washed crystals. No significant amount of protein was detected in the supernatant after the washing procedure. Furthermore, the pelleted crystals remained fully intact with no visible loss of crystal integrity after the catalytic assay (Figure 4C). The 5 nt substrate was efficiently cleaved by the protein crystals in the absence of Mn^{2+} ions (Figure 4D). Overall, these experiments suggest that the NendoU protein is catalytically active and intact within the crystals during and post catalysis.

Room-temperature SFX data collection of NendoU

In this study, the room temperature structure of NendoU was determined by SFX and resolved at a resolution of 2.6 Å. Data were collected at the MFX beamline at the LCLS. NendoU was crystallized by the batch method as well as a concentration procedure at low ionic strength. The crystal suspensions were left to settle overnight, and the crystal density was then adjusted to 1 part settled crystal pellet plus 3 parts supernatant. SFX data were collected at room temperature at 30 fs nominal pulse duration with a repetition rate of 120 Hz and a photon energy of 9.79 keV.

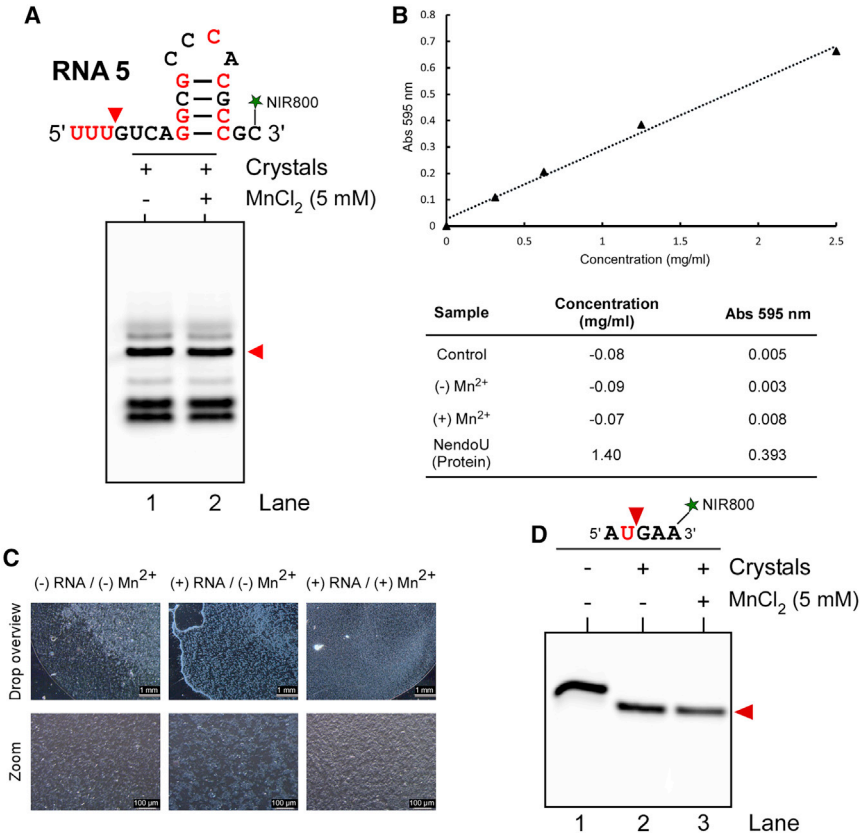

Sample	Concentration (mg/ml)	Abs 595 nm
Control	-0.08	0.005
(-) Mn^{2+}	-0.09	0.003
(+) Mn^{2+}	-0.07	0.008
NendoU (Protein)	1.40	0.393

Figure 4. Determining catalytic activity of NendoU crystals and crystal stability post catalysis

The crystals grown by the batch method in the presence of citrate were used for this experiment.

(A) Endoribonuclease assay of NendoU crystals for 21 nt RNA (substrate 5). Secondary structure model is shown above the RNA gel with the major cleavage site shown by red arrowheads above the RNA structure and at the gel.

(B) Bradford assay of supernatant from the crystal enzymatic assay to test crystal dissolution. The Bradford assay standard curve (top) with concentration determination of samples and control (bottom) are shown.

(C) Polarized microscopy images of crystals following in-crystal enzymatic cleavage reactions. Drop overview (top row) and zoom (bottom row) are shown with corresponding samples labeled above each column. Scale bars, 1 mm for the drop overview and 100 μm for the zoomed-in image.

(D) Endoribonuclease assays of NendoU crystals for the 5 nt RNA substrate. Sequence is shown above the RNA gel with the cleavage site shown by a red arrowhead above the RNA sequence and the cleavage product is also indicated by a red arrowhead beside the gel.

Representative diffraction patterns of a single microcrystal of NendoU delivered with, first, a gas dynamic virtual nozzle (GDVN) system in a helium environment and, second, the electrospinning co-microfluidic electrokinetic sample holder (MESH) injector operating in air are shown in Figure S3. The background contribution from the GDVN injector system (Figure S3A) operating in helium was markedly reduced compared with that of the co-MESH injection in air (Figure S3B). For direct comparison, a Bragg spot of similar intensity and scattering angle is enlarged in the insets. The peak intensities for both Bragg spots are on the order of 1,000 to 1,500 detector counts for the highest-intensity pixels, but significant differences in the respective background contributions are evident. The average background count/pixel was only 30–50 counts for the data collected in helium with the GDVN, whereas for the co-MESH injector the average background pixel count exceeded 300 counts for the data collection in air. However, despite the higher background contribution from the co-MESH injection setup, this system was chosen for collection of full datasets due to the achievable higher hit rates (a factor of 10 increase) with lower sample consumption.

Data collection statistics for the datasets collected with crystals grown from the two different crystallization procedures are shown in Table 1. Representative diffraction patterns are shown in Figure S4.

The crystals grown by batch with agitation diffract to a significantly higher resolution (2.6 Å) compared with those grown by concentration (4.4 Å resolution). Therefore, subsequent data processing and structure determination focused on the crystals grown by batch with agitation, and the refinement statistics for the structure solution are included in Table 1.

Room-temperature SFX structure of NendoU

Figure 5 shows the RT-SFX structure of NendoU determined at a resolution of 2.6 Å based on the SFX data collected from NendoU microcrystals grown in the citrate condition and delivered to the XFEL beam with the co-MESH injector system. NendoU formed a hexamer featuring a dimer of trimers (Figure 5B), which form a double ring assembly consisting of one homotrimer of monomer A and one homotrimer of monomer B. The asymmetric unit of the crystal assembly comprises one monomer of each trimer, termed "chain A" and "chain B" (Figure 5A). Our room-temperature (RT) structure is slightly elongated compared with the standard crystallography structure determined under cryogenic conditions (cryo-MX), which is also reflected in the slightly larger unit cell dimensions (4, 4, and 6 Å larger in the a, b, and c directions, respectively) (Figure 5C). More interestingly, the monomers are shifted slightly relative to one another, with the RT structure featuring a shift of the orientation of monomer B versus monomer A. This indicates that there is some flexibility between the two trimers in the hexamer at RT. The RT-SFX structure reflects the near-physiological state of NendoU, where the protein dynamics are more observable due to the increased flexibility at RT compared with cryogenic conditions. To investigate differences in the flexibility, Figures 5D and 5E show the RT-SFX

Table 1. NendoU data collection and refinement statistics for PDB entry 7K9P

	Batch with agitation (PDB: 7K9P)	Crystallization by concentration[a]
X-ray wavelength (Å)	1.277	1.277
Space group	P63	P63
No. indexed patterns	25,123	6,843
a, b, c (Å) α, β, γ (°)	153.4, 153.4, 116.8 90, 90, 120	153.6, 153.6, 117.9 90, 90, 120
Resolution (Å)	33.59–2.6 (2.69–2.6)	35.44–4.4 (4.49–4.4)
No. unique reflections	94,549 (9,443)	21,162 (2,645)
Redundancy	100 (70)	312 (236)
SNR	3.1 (0.2)	1.1 (0.2)
Completeness (%)	100 (100)	100 (100)
CC[a]	0.97 (0.23)	0.94 (0.20)
CC1/2	0.88 (0.03)	0.78 (0.02)
Structure refinement		
R_{work}	0.191	
R_{free}	0.201	
Mean isotropic B factor (Å^2)	47.7	
Wilson plot B factor (Å^2)	86.4	
No. atoms		
Protein	5,504	
Solvent	16	
Ligand	26	
RMSD, bond lengths (Å)	0.006	
RMSD, angles (°)	1.034	
Ramachandran plot (%)		
Favored	94.94	
Allowed	4.19	
Outliers	0.87	

[a]Due to low resolution the structure was not refined and deposited in the PDB.

and the cryo-MX structure by Kim et al.[7] colored by the respective atomic B factors after structural refinement.

The SFX structure had, overall, higher B-factor values than the cryo-MX structure. This is expected, as molecular motions are more constrained under cryogenic conditions, while RT allows for higher flexibility of the protein molecules. Thereby, the serial crystallography RT structural data represent a state of NendoU that is closer to physiological conditions than would be found for cryogenic structures. However, the NendoU molecules of both the cryo-MX and the SFX structures feature a dominant difference in the flexibility of the structures of chain A compared with chain B. The NendoU molecules in the lower trimer (chain A, Figure 5) are more rigid than in the upper trimer (chain B, Figure 5). The difference in flexibility of the respective trimers is exacerbated by the RT conditions for the SFX structure, which also explains the shifted orientation in the SFX structure compared with the cryo-MX structure.

Differences in the citrate binding sites between the two trimers of NendoU

A comparison of the electron-density omit maps (contoured at 3 σ) of the citrate molecule located in the binding sites of the two monomers of NendoU in the asymmetric unit is shown in Figure 6. At first glance, the maps for the citrate molecule in the binding site of chain A are better defined than those of chain B, which may be reflective of the higher flexibility of chain B versus chain A. Furthermore, the conformation and hydrogen bonding network for the citrate molecule are different between the two binding sites after refinement. In the binding site of chain A, the citrate is more tightly connected through a more complex hydrogen bonding network compared with that observed in chain B. To confirm the results, we also calculated POLDER maps that are shown in Figure S5.

Comparison of SFX and cryo-EM structures

To further investigate the asymmetry in the respective trimers, a comparison with the published cryo-EM structure was conducted. We would like to acknowledge that this was facilitated by M. Frazier and R. Stanley kindly providing us with the half-map data for their pre-cleavage structure from Frazier et al.[6] Figure 7 (top) shows the cryo-EM electron-density maps for one monomer of each trimer (termed A, B, and C for trimer 1 and D, E, and F for trimer 2 in their publication and corresponding PDB model) contoured at the same level, superimposed on

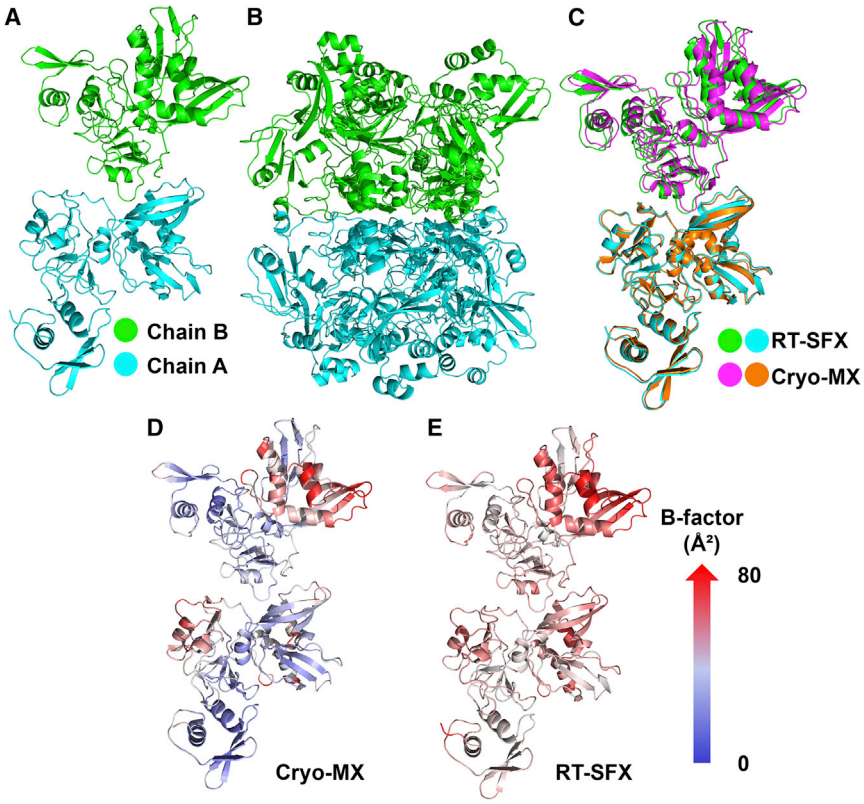

Figure 5. Room-temperature SFX structure of NendoU

(A) Structure of the two monomers in the asymmetric unit: monomer A (chain A) is depicted in blue and monomer B (chain B) is depicted in green.

(B) Structure of the hexamer, a dimer of trimers, with the top trimer in green (chain B) and the lower trimer in blue (chain A).

(C) Overlay of the RT-SFX structure of NendoU (this work; PDB: 7K9P in blue/green) with the structure determined by Kim et al.[7] by standard crystallography under cryogenic conditions (PDB: 6W01) in orange/pink.

(D) B factors of the cryo-MX structure (PDB: 6W01) of NendoU. Cartoon representation of the protein, colored with the lowest B factors (i.e., least flexible domains) depicted in blue and highest B factors (i.e., highest flexibility domains) depicted in red. The color gradient is scaled from 0 to 80 Å^2, with the darkest red having a B factor of 80 Å^2.

(E) B factors of the RT-SFX structure (PDB: 7K9P; this work) of NendoU. The color scale for the B factors is identical to that of (D).

their corresponding structure depicted in sticks. The superiority of the cryo-EM density map for the trimer consisting of their subunits D, E, and F indicates that this is the trimer corresponding to the less flexible trimer in our structure (made up of the monomers chain A) and that subunits A, B, and C correspond to chain B in our structure. This was, therefore, the chosen configuration for alignment to our structure, with RMSD values (all atoms in the chain) of 1.16 (1.079 for Cαs only) for the less flexible trimer and 1.223 (1.20 for Cαs only) for the more flexible NendoU molecule B. In Figure 7 (middle), the electron density (contoured at 1.0 σ) of our RT-SFX structure is depicted for the active-site residues (235–238, 245–250, 289–295, 341–344), in contrast to the cryo-EM maps from Frazier et al.[6] (bottom). All three structures compared in this article are superimposed (for the cryo-MX structure, RMSD values are chain A, 1.049 and 0.932, and chain B, 0.940 and 1.020, for all atom and Cα alignment, respectively). Both RT-SFX maps, as well as the cryo-EM maps, have more detail in the chain A map (see, for example, PHE342), re-affirming that this trimer is less flexible than the trimer comprising chain B molecules in both cases. It can clearly be seen that the active-site configurations for the RT (cyan) and cryo-MX (orange) structures are in good agreement with the cryo-EM structure (green). One noticeable difference, however, is the different placement of HIS235 in both crystallography structures with respect to the cryo-EM structure. While the electron density from the RT-SFX data is clearly defined around this residue, the cryo-EM density is not, which would account for the differing refinement results. Frazier et al. predicted that HIS235 forms a hydrogen bond to their modified RNA substrate in the pre-cleavage structure, whereas from Figure 6 it can be seen that HIS235 forms a hydrogen bond to the citrate occupying the active site in our RT-SFX structure.[6] Since the cryo-MX structure also contains citrate in the active site, it is conceivable that this bond constrains the motion of HIS235 in the crystallography structures. The lack of electron density for this residue in the cryo-EM maps indicates that it is more flexible and occupies a range of confirmations and therefore plays a key role in substrate binding.

DISCUSSION

Established prerequisite findings for future TR-SFX experiments

The SARS-CoV-2 endoribonuclease, NendoU, has become a focal point of structural studies in COVID-19 research due to the role of this enzyme in viral evasion of the host immune system. Structural studies demonstrate the high conservation of structural features between SARS-CoV, MERS-CoV, and SARS-CoV-2, which makes it a promising drug target against coronaviruses. This work describes the RT structure determination of NendoU by SFX at an XFEL, which paves the way for future TR-SFX studies by establishing prerequisite conditions and methodologies. Further, it also offers new understanding of the dynamics of NendoU for applications to drug discovery.

To accomplish time-resolved studies, initial conditions for successful SFX experiments were identified. Both *in vivo* and *in vitro* expression systems for NendoU have been established, and large-scale isolation and purification procedures were developed to enable future time-resolved studies, which require notoriously large sample amounts. Previously, NendoU proved to be toxic during overexpression in *E. coli*. Over 300 L of *E. coli* could be grown and purified to produce roughly 250 mg of protein to enable SFX experiments. However, a further

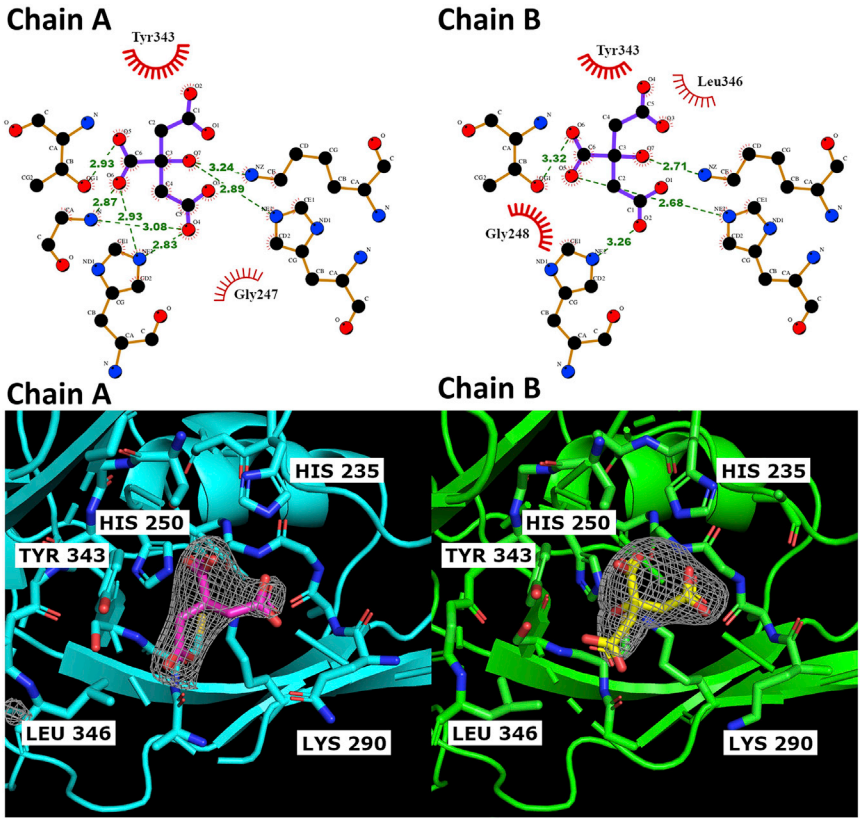

Figure 6. Differences in binding sites of citrate in the RT-SFX structure

(Top) Ligand plot analyses of the citrate molecules in both active sites. Note that the orientation and hydrogen bonding network are different for citrate in chains A and B, with a closer hydrogen bonding network of citrate identified in the low-flexibility molecule A compared with that of molecule B. (Bottom) Omit map comparison of electron density (Fo-Fc map) of citrate in the binding sites (contoured at 3.0 σ) of the more rigid molecule A and the more flexible NendoU molecule B. Note that the electron density for citrate is better defined in the rigid molecule A than in the more flexible molecule B.

increase in cell culture capacity may be required for time-resolved experiments due to increased protein demands for longer experiments (collection of multiple reaction time points), which will be very challenging in terms of production costs and labor. The cell-free expression of NendoU was therefore explored, offering a long-term solution for protein production for such studies. Cell-free expression is a flexible and increasingly cost-effective one-pot *in vitro* expression approach, in which the cell's translational machinery is provided in a cell lysate that is combined with the target cDNA. The expression is promoted by supplementing the reaction with amino acids and any necessary additives. This mitigates cell viability concerns while enabling a highly tunable expression platform.[34] High yields of NendoU could be expressed *in vitro* using this cell-free approach. Further optimization of expression yield and translation product purity may be achieved through modifications of the expression vector and variation of the expression conditions to further promote hexamer stability.

Based on the 2D structure prediction of the negative-strand RNA of NendoU from SARS-CoV-2, we have designed 5 and 21 nt substrates that mimic the 5′ end of the RNA after the poly(U) leader. For both substrates, we established functional assays that confirmed that NendoU rapidly cleaves the small and large RNA substrates both in solution and in crystals. The design and functional studies of multiple-length RNAs coupled with optimized microcrystallization conditions performed at an XFEL provide the foundation for future time-resolved studies of NendoU. The two microcrystallization methods explored in this study have different merits. The first approach, batch with agitation, enabled the production of large quantities of crystals and high-resolution data collection for the RT structure. However, this method led to crystals containing citrate, which occupies the binding site, and thus would be suboptimal for mix-and-inject studies. Following the NendoU beamtime, crystals were optimized into two conditions without citrate, which diffracted comparable to the crystals grown in the presence of citrate during a subsequent LCLS PCS screening beamtime (data not shown). While we show that the crystals are still active despite the citrate occupying the binding site, competing occupancy for initial mix-and-inject experiments is less than ideal, and thus we favor a citrate-free crystallization condition. In an alternative approach, crystallization by concentration, protein crystallizes in the respective buffer without the addition of a precipitant. These low-salt conditions are preferable for RNA binding and would therefore be more favorable for mix-and-inject studies if the diffraction resolution could be improved. Alternatively, crystals grown in batch, but without the addition of citrate, are introduced as potential candidates for future time-resolved studies. Time-resolved studies of NendoU could reveal critical insights into how docking, cleavage, and substrate release are achieved by NendoU.

One potential reason for the difficulty in capturing structures of NendoU bound to RNA is the unstable nature of longer RNAs that are subject to degradation, prohibiting longer incubation with NendoU prior to data collection. This may explain why the shorter incubations used in preparing cryo-EM samples (1 h) have been more productive than attempts at standard cryogenic crystallography that can require hours or even days depending on the preparation method. TR-SFX experiments using the mix-and-inject method will enable shorter incubation times to capture the catalytic reaction of NendoU: SFX allows for diffraction of nanocrystals and small microcrystals, with shorter diffusion pathways resulting in faster diffusion times (and hence reaction initiation) of the RNA into the crystals.[27]

An important requirement for TR-SFX studies is that the substrates diffuse into the crystal and the catalytic sites are accessible to the substrates via solvent channels. We therefore

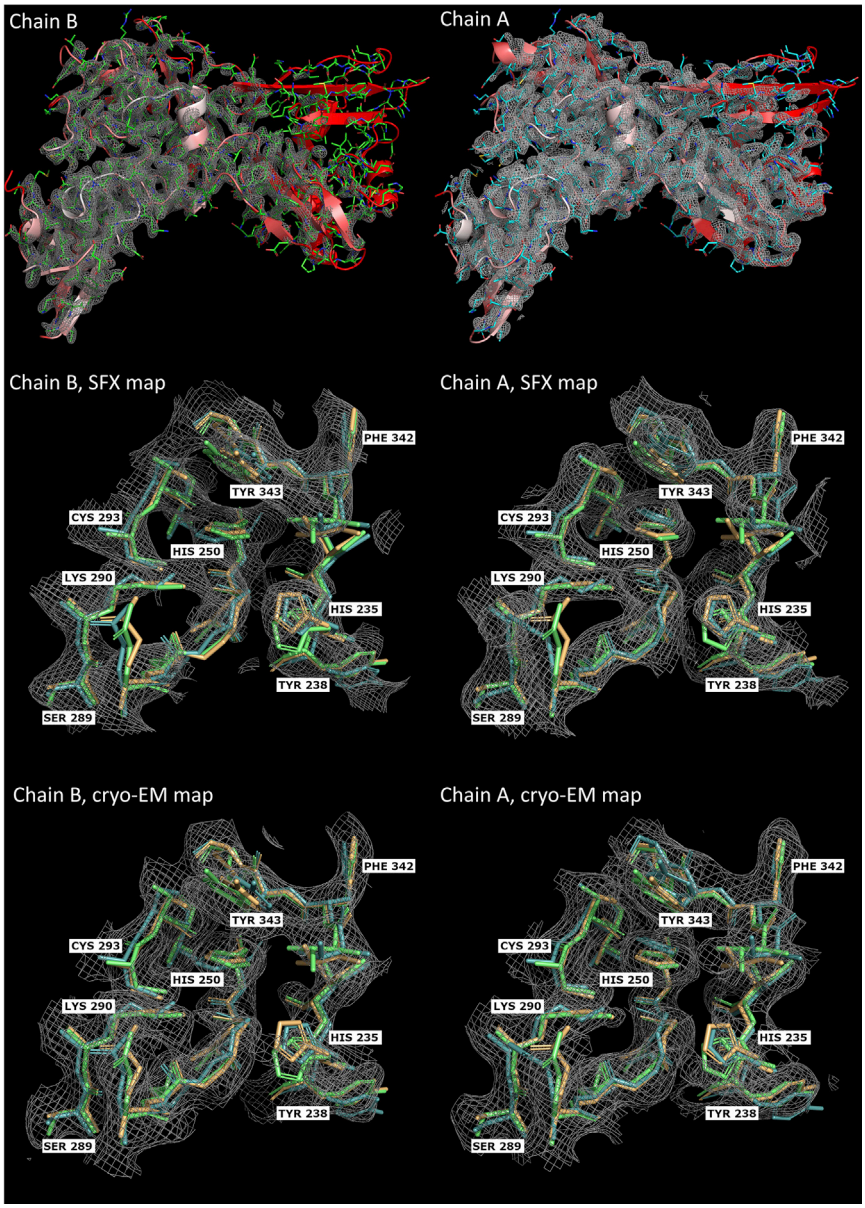

Figure 7. Comparison of the RT-SFX and the cryo-EM structures

(Top) Chain A and B pre-cleavage cryo-EM maps from Frazier et al.[6] (EMDB: 24137) for one monomer making up the respective trimers, contoured at the same contour level. Our RT crystal structure is depicted as a ribbon model (colored by B factor), superimposed on the cryo-EM model for the respective subunits A (green) and D (blue) from PDB: 7N33. (Middle) Structural superposition of the active-site residues for all of the structures discussed in this study along with the SFX electron-density map contoured at 1.0 σ. (Bottom) Cryo-EM map. The active-site residues for the RT-SFX structure (PDB: 7K9P in cyan), the pre-cleavage cryo-EM structure (PDB: 7N33 in green), and the cryo-MX structure (PDB: 6W01 in orange) are shown with the electron-density map calculated for the RT-SFX structure (top) contoured at 1.0 σ and the cryo-EM map (bottom) for each respective monomer.

analyzed the crystal packing and the size of the solvent channels in the NendoU crystals as shown in Figure S6. The NendoU crystals contain wide solvent channels of ~100 Å that could allow even very large substrates to diffuse into the crystals. This explains why the 21 nt RNA is able to reach the respective catalytic site and is cleaved within the crystals. Even more importantly, both catalytic sites in the A and B chains are fully exposed to the solvent channels. This further supports that NendoU remains highly active in crystal form, cleaving the large RNA substrates of 5 and 21 nt, which mimic the 5′ end of the SARS-CoV-2 negative-strand RNA. This may also contribute to the unique finding that NendoU crystals could cleave RNA without the presence of manganese. While manganese independence has been reported in the NendoU equivalent of other coronaviruses, the case for SARS-CoV-2 NendoU is unclear. While manganese has never been observed in the structure, it is believed to play a role in RNA coordination. To expand on this, we hypothesize it may have subtle impacts on the NendoU hexamer that promote activity. This would explain why activity is still seen when NendoU is crystallized, with crystal packing supporting the hexameric arrangement while allowing substrate to diffuse into the large solvent channels. The fact that catalytic activity is preserved in NendoU crystals and the catalytic sites are fully accessible to the solvent channels is ideal for future TR-SFX studies with the ultimate goal of determining a molecular "movie" of the catalytic mechanism of NendoU.

Structural insights and molecular basis for intrinsic flexibility of NendoU

Our initial observations were that the catalytic site in chain A is more exposed to solvent, while the catalytic site in chain B is more secluded (Figure S6). The B-factor analysis and the network of hydrogen bonds suggest that the catalytic site of chain B is more flexible than the chain A site and binds citrate less tightly. The higher flexibility of chain B (the upper trimer in Figure 8A) and its catalytic site compared with chain A is not caused by restrictions in crystal contacts; thus, our hypothesis is that this higher flexibility is an intrinsic feature of the NendoU protein and its catalytic cycle. This effect was not unexpected and has also been seen in other protein structures in which both the SFX and the cryo-MX structures have been determined.[35]

To investigate this phenomenon further, we compared our SFX structure with the recently determined cryo-EM structure of NendoU with bound RNA.[6,21] In both structures, RNA could be identified in only one of the two trimers. While the cryo-EM structure showed some density in the catalytic sites of the other

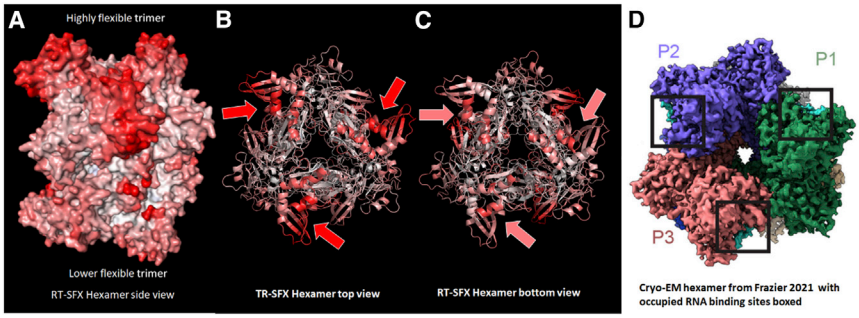

Figure 8. Flexibility analysis of the RT-SFX dimer of trimers of NendoU in comparison with the cryo-EM structure with nucleotides bound in the P1, P2, and P3 monomers in the trimer

(A) Surface model of the TR-SFX structure of the NendoU hexamer colored by B factor (blue, low B factors; pink, medium B factors; red high B-factors).

(B) Depiction of the backbone of the RT-SFX trimer viewed from the top, where the catalytic sites show high B factors (red arrows).

(C) Bottom view, where the catalytic sites show medium B factors (pink arrows).

(D) Cryo-EM structure from Frazier et al.[6] with the view from the bottom on the trimer, which has nucleotides bound in the three catalytic sites, P1, P2, and P3.

trimer, it could not be definitively identified as nucleotides. They therefore applied C3 symmetry and built their structural model with nucleotides in only one of the two trimers.[6] This interesting result, combined with our data, indicates that the different flexibilities for the two trimers in the NendoU hexamer is an intrinsic and very likely functionally important feature of NendoU. This poses two major questions: (1) why would only one of the two trimers bind and cleave substrate and (2) why is the hexamer required for catalytic activity?

While advancements have been made in understanding the role of the catalytic domain, we propose a broader mechanism addressing substrate docking and release as it relates to the dimer of trimer formation of NendoU. The importance of NendoU has long been established across the *Coronaviridae* family, and disruption of the oligomer is detrimental for activity, with particular sensitivity in the middle and N-terminal domains.[7] This likely contributes to the high conservation across coronaviruses and limited mutation in SARS-CoV-2 variants compared with other proteins, such as the spike protein. Mutational studies of NendoU from SARS-CoV suggest that an allosteric switching mechanism is triggered by the formation of the hexamer, which supports neighboring catalytic domains and turns on activity once the units are assembled.[9]

Based on our structure and flexibility analysis, we hypothesize that NendoU may catalyze cleavage of the coronaviral negative-strand RNA through a binding change mechanism. In this model, shown in Figure 9, the affinity of the substrate would alternate between the trimers in the hexamer. The substrate would be bound only to the high-affinity trimer that would correspond to the A trimer (bottom) in our structure, while the B-site trimers feature a high flexibility and therefore do not bind the substrate. This hypothesis would correlate well with the pre- and post-cleavage cryo-EM structures that show preferential binding of ssRNA to only one trimer and explain why the catalytic site is empty in the second trimer.[6] Upon substrate cleavage and release in the top trimer, the catalytic sites in the bottom trimer would change their conformation and tightly bind the substrate and catalyze the next round of RNA cleavage.

In this mechanism, binding affinity would alternate between the trimers, driven by the cleavage of the substrate and transforming the tight-binding site into a low-affinity site, allowing for the release of the products. Simultaneously, the previously loose-binding site would become less flexible and bind the substrate tightly. The interplay between the trimers would occur via the interface between the trimers, with differences in flexibility across the hexamer corresponding to substrate docking, cleavage, and release. This would further explain the importance of the hexamer for activity and account for the difference in NendoU flexibility across the asymmetric unit in both the SFX and the cryo-cooled crystal structures.[7] In addition, analysis of the conformational landscapes of NendoU in cryo-EM indicates that the presence of a single nucleotide creates a fixed position for the catalytic domain, while in its absence, there is a wobble in the domain.[21] This relates to the proposed mechanism that the flexibility of NendoU corresponds with substrate binding.

Finally, the recently published cryo-EM structure of NendoU bound to a 52 nt dsRNA provides support for a hypothesized RNA binding groove that spirals around the SARS-CoV-2 NendoU hexamer, interacting with both trimers.[13,18] This supports the hypothesis (depicted in Figure 9) that only one trimer can be active, especially in processing dsRNA, so that after product release the lower trimer is no longer able to perform substrate cleavage when substrate is bound to the top trimer molecules. This functional binding-change model would explain why (1) the hexamer is essential for the function, (2) only one trimer contains RNA in the cryo-EM structure, and (3) strong intrinsic differences were observed in flexibility between the two trimers.

Outlook

TR-SFX studies would enable direct observation of the catalytic mechanism, as well as the detection of changes in flexibility during substrate docking and release across the hexamer. These insights would aid in the development of NendoU-targeted therapeutics. Because the time scale for RNA docking and catalysis is very controversial in the literature, we intend to collect full datasets spanning time delays of 10 ms up to 5 s. Based on these results, finer time slicing in the time range where the catalytic reaction occurs, and thereby the largest conformational changes occur, can be targeted. Ideally, we would use optimized crystals grown at low ionic strength for these experiments to promote RNA binding. We have already confirmed that these crystals have the same unit cell and crystal packing as the citrate crystals and therefore also contain the large solvent channels. As the virus continues to evolve, understanding how mutations in variants of interest affect flexibility and hexamer formation can provide

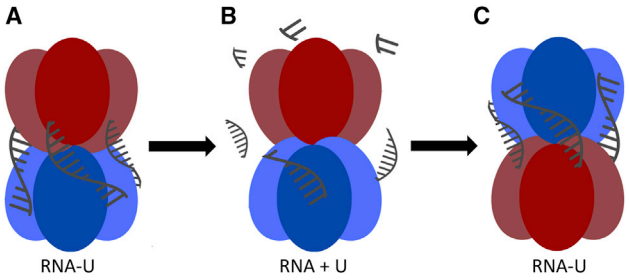

Figure 9. Schematic of the proposed binding-change mechanism for the function of U-RNA hydrolysis by hexameric NendoU

The hexamer is depicted in a side view.

(A) The bottom trimer with low flexibility (blue) has the U-RNA substrate bound in its tight binding sites. The binding sites of the highly flexible trimer (red) have a lower binding affinity and are empty.

(B) Cleavage of U-RNA into U + RNA provides the energy for a change in binding affinity, where the bottom trimers become highly flexible (red), lowering the binding affinity and leading to the products U and RNA. The top trimer becomes less flexible (blue) and its substrate binding site changes to high affinity.

(C) U-RNA binds to the high-affinity binding sites of the top trimer, initiating the next round of the cycle.

insight into the function of these mutations. Antivirals that limit the flexibility and oligomerization of NendoU by blocking the allosteric switch may provide a promising alternative to inhibiting NendoU activity via the active site. The flexibility of NendoU seen in the RT-SFX structure reported here is an important feature in obtaining a more complete picture of the function and dynamics of the protein, and the approaches delineated are critical steps needed for pursuing time-resolved crystallographic studies.

STAR★METHODS

Detailed methods are provided in the online version of this paper and include the following:

- KEY RESOURCES TABLE
- RESOURCE AVAILABILITY
  - Lead contact
  - Materials availability
  - Data and code availability
- EXPERIMENTAL MODEL AND SUBJECT DETAILS
- METHOD DETAILS
  - Vector design and cloning
  - *In vivo* expression of NendoU protein
  - Development of an *in vitro* expression system for NendoU protein
  - Large scale protein purification of NendoU
  - Crystallization of NendoU protein
  - RNA substrate design and functional assays
  - X-ray diffraction data collection and analysis
- QUANTIFICATION AND STATISTICAL ANALYSIS

SUPPLEMENTAL INFORMATION

Supplemental information can be found online at https://doi.org/10.1016/j.str.2022.12.009.

ACKNOWLEDGMENTS

We are very grateful for all the people who supported the experiment at LCLS by being present in person and participating remotely during the onset of the COVID-19 pandemic in August 2020. We acknowledge LCLS at SLAC for the provision of RAPID ACCESS X-ray free-electron laser beamtime at the MFX scientific instrument and would like to thank all staff members of LCLS for their strong support. We would further like to thank Robin Stanley and Meredith Frazier for providing access to their cryo-EM maps. We also thank Oleksandr Yefanov for providing detector geometry files.

This work was supported by two RAPID grant awards from the National Science Foundation, "IIBR: Instrumentation: Time-resolved studies of the SARS-CoV-2 endonuclease NP15" (award 2031343) and "Structure, function and dynamics of SARS Coronavirus-2 main protease 3CLpro determined with mix-and-inject serial XFEL crystallography" (award 2030466). The work was also supported by the NSF Science and Technology Center award "Biology with X-ray lasers (BioXFEL)" (award 1231306). D.L. was supported by NIH grant R01GM094450. J.M.M-G. was funded by the Community of Madrid through an "Atracción y retención de talento" grant (2019-T1/BMD-15552). The work was also supported by funds from National Institutes of Health grants R01GM095583 and 5R01GM117342, by the Biodesign Center for Applied Structural Discovery at ASU, and the US Department of Energy through Lawrence Livermore National Laboratory under contract DE-AC52-07NA27344. Use of the LCLS, SLAC National Accelerator Laboratory, is supported by the US Department of Energy, Office of Science, Office of Basic Energy Sciences under contract DE-AC02-76SF00515.

AUTHOR CONTRIBUTIONS

Experimental design, P.F., S. Botha, A.R., and J.J-L.C.; *in vitro* expression and purification, M.L.S., M.A.C., and M.F.; *in vivo* expression, R.J.J., M.Z.S., E.K.K., N.N., and M.C.Y.; plasmid design, D.T.H. and M.C.Y.; *in vitro* purification, R.J.J., J-H.Y., N.N., and M.Z.S.; crystallization, J.M.M-G., R.J.J., P.F., N.N., and D.L.; analysis of the RNA sequences and design of the RNA substrates, J.J-L.C.; RNA assays, D.L., J.J-L.C., N.N., and R.J.J.; XFEL data collection at LCLS, R.J.J., P.F., D.D., M. Sonker, B.H., R.G.S., M.S.H., S.L., A.B., C.K., S. Boutet, S. Botha, G.K., T.D.G., V.M., A.T., R.F., M. Schmidt, M.F., and M.A.Z.; microfluidics/injection, D.D., M. Sonker, M.T.R., S.L., R.N., R.A.K., and R.G.S.; beamline operation, B.H., R.G.S., M.S.H., S.L., A.B., C.K., and S. Boutet; XFEL data analysis, S. Botha, G.K., T.D.G., V.M., A.T., and M. Schmidt; writing and editing of the manuscript, all authors.

DECLARATION OF INTERESTS

The authors declare no competing interests.

INCLUSION AND DIVERSITY

We support inclusive, diverse, and equitable conduct of research.

Received: July 28, 2022
Revised: October 8, 2022
Accepted: December 14, 2022
Published: January 10, 2023

REFERENCES

1. Hackbart, M., Deng, X., and Baker, S.C. (2020). Coronavirus endoribonuclease targets viral polyuridine sequences to evade activating host sensors. Proc. Natl. Acad. Sci. USA *117*, 8094–8103. https://doi.org/10.1073/pnas.1921485117.
2. Kindler, E., Gil-Cruz, C., Spanier, J., Li, Y., Wilhelm, J., Rabouw, H.H., Züst, R., Hwang, M., V'Kovski, P., Stalder, H., et al. (2017). Early endonuclease-mediated evasion of RNA sensing ensures efficient coronavirus replication. PLoS Pathog. *13*, e1006195. https://doi.org/10.1371/journal.ppat.1006195.
3. Deng, X., Hackbart, M., Mettelman, R.C., O'Brien, A., Mielech, A.M., Yi, G., Kao, C.C., and Baker, S.C. (2017). Coronavirus nonstructural protein 15

mediates evasion of dsRNA sensors and limits apoptosis in macrophages. Proc. Natl. Acad. Sci. USA *114*, E4251–E4260. https://doi.org/10.1073/pnas.1618310114.

4. Gao, B., Gong, X., Fang, S., Weng, W., Wang, H., Chu, H., Sun, Y., Meng, C., Tan, L., Song, C., et al. (2021). Inhibition of anti-viral stress granule formation by coronavirus endoribonuclease nsp15 ensures efficient virus replication. PLoS Pathog. *17*, e1008690. https://doi.org/10.1371/journal.ppat.1008690.

5. Beyer, D.K., and Forero, A. (2022). Mechanisms of antiviral immune evasion of SARS-CoV-2. J. Mol. Biol. *434*, 167265. https://doi.org/10.1016/j.jmb.2021.167265.

6. Frazier, M.N., Dillard, L.B., Krahn, J.M., Perera, L., Williams, J.G., Wilson, I.M., Stewart, Z.D., Pillon, M.C., Deterding, L.J., Borgnia, M.J., and Stanley, R.E. (2021). Characterization of SARS2 Nsp15 nuclease activity reveals it's mad about U. Nucleic Acids Res. *49*, 10136–10149. https://doi.org/10.1093/nar/gkab719.

7. Kim, Y., Jedrzejczak, R., Maltseva, N.I., Wilamowski, M., Endres, M., Godzik, A., Michalska, K., and Joachimiak, A. (2020). Crystal structure of Nsp15 endoribonuclease NendoU from SARS-CoV-2. Protein Sci. *29*, 1596–1605. https://doi.org/10.1002/pro.3873.

8. Guarino, L.A., Bhardwaj, K., Dong, W., Sun, J., Holzenburg, A., and Kao, C. (2005). Mutational analysis of the SARS virus Nsp15 endoribonuclease: identification of residues affecting hexamer formation. J. Mol. Biol. *353*, 1106–1117. https://doi.org/10.1016/j.jmb.2005.09.007.

9. Joseph, J.S., Saikatendu, K.S., Subramanian, V., Neuman, B.W., Buchmeier, M.J., Stevens, R.C., and Kuhn, P. (2007). Crystal structure of a monomeric form of severe acute respiratory syndrome coronavirus endonuclease nsp15 suggests a role for hexamerization as an allosteric switch. J. Virol. *81*, 6700–6708. https://doi.org/10.1128/JVI.02817-06.

10. Mushegian, A., Sorokina, I., Eroshkin, A., and Dlakić, M. (2020). An ancient evolutionary connection between Ribonuclease A and EndoU families. RNA *26*, 803–813. https://doi.org/10.1261/rna.074385.119.

11. Kim, Y., Wower, J., Maltseva, N., Chang, C., Jedrzejczak, R., Wilamowski, M., Kang, S., Nicolaescu, V., Randall, G., et al. (2021). Tipiracil binds to uridine site and inhibits Nsp15 endoribonuclease NendoU from SARS-CoV-2. Commun. Biol. *4*, 193–211. https://doi.org/10.1038/s42003-021-01735-9.

12. Perry, J.K., Appleby, T.C., Bilello, J.P., Feng, J.Y., Schmitz, U., and Campbell, E.A. (2021). An atomistic model of the coronavirus replication-transcription complex as a hexamer assembled around nsp15. J. Biol. Chem. *297*, 101218. https://doi.org/10.1016/j.jbc.2021.101218.

13. Frazier, M.N., Wilson, I.M., Krahn, J.M., Butay, K.J., Dillard, L.B., Borgnia, M.J., and Stanley, R.E. (2022). Flipped over U: structural basis for dsRNA cleavage by the SARS-CoV-2 endoribonuclease. Preprint at bioRxiv. https://doi.org/10.1101/2022.03.02.480688.

14. Bhardwaj, K., Guarino, L., and Kao, C.C. (2004). The severe acute respiratory syndrome coronavirus Nsp15 protein is an endoribonuclease that prefers manganese as a cofactor. J. Virol. *78*, 12218–12224. https://doi.org/10.1128/JVI.78.22.12218-12224.2004.

15. Ivanov, K.A., Hertzig, T., Rozanov, M., Bayer, S., Thiel, V., Gorbalenya, A.E., and Ziebuhr, J. (2004). Major genetic marker of nidoviruses encodes a replicative endoribonuclease. Proc. Natl. Acad. Sci. USA *101*, 12694–12699. https://doi.org/10.1073/pnas.0403127101.

16. Frazier, M.N., Wilson, I.M., Krahn, J.M., Butay, K.J., Dillard, L.B., Borgnia, M.J., and Stanley, R.E. (2022). Flipped over U: structural basis for dsRNA cleavage by the SARS-CoV-2 endoribonuclease. Nucleic Acids Res. *50*, 8290–8301. https://doi.org/10.1093/nar/gkac589.

17. Wilson, I.M., Frazier, M.N., Li, J.L., Randall, T.A., and Stanley, R.E. (2022). Biochemical characterization of emerging SARS-CoV-2 Nsp15 endoribonuclease variants. Preprint at bioRxiv. https://doi.org/10.1101/2022.05.10.491349.

18. Bhardwaj, K., Sun, J., Holzenburg, A., Guarino, L.A., and Kao, C.C. (2006). RNA recognition and cleavage by the SARS coronavirus endoribonuclease. J. Mol. Biol. *361*, 243–256. https://doi.org/10.1016/j.jmb.2006.06.021.

19. Canal, B., Fujisawa, R., McClure, A.W., Deegan, T.D., Wu, M., Ulferts, R., Weissmann, F., Drury, L.S., Bertolin, A.P., Zeng, J., et al. (2021). Identifying SARS-CoV-2 antiviral compounds by screening for small molecule inhibitors of nsp15 endoribonuclease. Biochem. J. *478*, 2465–2479. https://doi.org/10.1042/BCJ20210199.

20. Choi, R., Zhou, M., Shek, R., Wilson, J.W., Tillery, L., Craig, J.K., Salukhe, I.A., Hickson, S.E., Kumar, N., James, R.M., et al. (2021). High-throughput screening of the ReFRAME, Pandemic Box, and COVID Box drug repurposing libraries against SARS-CoV-2 nsp15 endoribonuclease to identify small-molecule inhibitors of viral activity. PLoS One *16*, e0250019. https://doi.org/10.1371/journal.pone.0250019.

21. Pillon, M.C., Frazier, M.N., Dillard, L.B., Williams, J.G., Kocaman, S., Krahn, J.M., Perera, L., Hayne, C.K., Gordon, J., Stewart, Z.D., et al. (2021). Cryo-EM structures of the SARS-CoV-2 endoribonuclease Nsp15 reveal insight into nuclease specificity and dynamics. Nat. Commun. *12*, 636. https://doi.org/10.1038/s41467-020-20608-z.

22. Olmos, J.L., Jr., Pandey, S., Martin-Garcia, J.M., Calvey, G., Katz, A., Knoska, J., Kupitz, C., Hunter, M.S., Liang, M., Oberthuer, D., et al. (2018). Enzyme intermediates captured "on the fly" by mix-and-inject serial crystallography. BMC Biol. *16*, 59. https://doi.org/10.1186/s12915-018-0524-5.

23. Kupitz, C., Olmos, J.L., Jr., Holl, M., Tremblay, L., Pande, K., Pandey, S., Oberthür, D., Hunter, M., Liang, M., et al. (2017). Structural enzymology using X-ray free electron lasers. Struct. Dyn. *4*, 044003. https://doi.org/10.1063/1.4972069.

24. Pandey, S., Calvey, G., Katz, A.M., Malla, T.N., Koua, F.H.M., Martin-Garcia, J.M., Poudyal, I., Yang, J.-H., Vakili, M., et al. (2021). Observation of substrate diffusion and ligand binding in enzyme crystals using high-repetition-rate mix-and-inject serial crystallography. IUCrJ *8*, 878–895. https://doi.org/10.1107/S2052252521008125.

25. Barty, A., Caleman, C., Aquila, A., Timneanu, N., Lomb, L., White, T.A., Andreasson, J., Arnlund, D., Bajt, S., Barends, T.R.M., et al. (2012). Self-terminating diffraction gates femtosecond X-ray nanocrystallography measurements. Nat. Photonics *6*, 35–40. https://doi.org/10.1038/nphoton.2011.297.

26. Chapman, H.N., Fromme, P., Barty, A., White, T.A., Kirian, R.A., Aquila, A., Hunter, M.S., Schulz, J., DePonte, D.P., Weierstall, U., et al. (2011). Femtosecond X-ray protein nanocrystallography. Nature *470*, 73–77. https://doi.org/10.1038/nature09750.

27. Schmidt, M. (2013). Mix and inject: reaction initiation by diffusion for time-resolved macromolecular crystallography. Adv. Condens. Matter Phys. *2013*, 1–10. https://doi.org/10.1155/2013/167276.

28. Pandey, S., Bean, R., Sato, T., Poudyal, I., Bielecki, J., Cruz Villarreal, J., Yefanov, O., Mariani, V., White, T.A., Kupitz, C., et al. (2020). Time-resolved serial femtosecond crystallography at the European XFEL. Nat. Methods *17*, 73–78. https://doi.org/10.1038/s41592-019-0628-z.

29. Ishigami, I., Lewis-Ballester, A., Echelmeier, A., Brehm, G., Zatsepin, N.A., Grant, T.D., Coe, J.D., Lisova, S., Nelson, G., Zhang, S., et al. (2019). Snapshot of an oxygen intermediate in the catalytic reaction of cytochrome c oxidase. Proc. Natl. Acad. Sci. USA *116*, 3572–3577. https://doi.org/10.1073/pnas.1814526116.

30. Stagno, J.R., Liu, Y., Bhandari, Y.R., Conrad, C.E., Panja, S., Swain, M., Fan, L., Nelson, G., Li, C., Wendel, D.R., et al. (2017). Structures of riboswitch RNA reaction states by mix-and-inject XFEL serial crystallography. Nature *541*, 242–246. https://doi.org/10.1038/nature20599.

31. Xu, X., Zhai, Y., Sun, F., Lou, Z., Su, D., Xu, Y., Zhang, R., Joachimiak, A., Zhang, X.C., Bartlam, M., and Rao, Z. (2006). New antiviral target revealed by the hexameric structure of mouse hepatitis virus nonstructural protein nsp15. J. Virol. *80*, 7909–7917. https://doi.org/10.1128/JVI.00525-06.

32. Andrews, R.J., Peterson, J.M., Haniff, H.S., Chen, J., Williams, C., Grefe, M., Disney, M.D., and Moss, W.N. (2020). An in silico map of the SARS-CoV-2 RNA Structurome. Preprint at bioRxiv. https://doi.org/10.1101/2020.04.17.045161.

33. Hunter, M.S., and Fromme, P. (2011). Toward structure determination using membrane–protein nanocrystals and microcrystals. Methods *55*, 387–404. https://doi.org/10.1016/j.ymeth.2011.12.006.

34. Lu, Y. (2017). Cell-free synthetic biology: engineering in an open world. Synth. Syst. Biotechnol. *2*, 23–27. https://doi.org/10.1016/j.synbio.2017.02.003.

35. Liu, W., Wacker, D., Gati, C., Han, G.W., James, D., Wang, D., Nelson, G., Weierstall, U., Katritch, V., Barty, A., et al. (2013). Serial femtosecond crystallography of G protein-coupled receptors. Science *342*, 1521–1524. https://doi.org/10.1126/science.1244142.

36. Makowska-Grzyska, M., Kim, Y., Maltseva, N., Li, H., Zhou, M., Joachimiak, G., Babnigg, G., and Joachimiak, A. (2014). Protein production for structural genomics using E. coli expression. In Structural Genomics and Drug Discovery (Springer), pp. 89–105. https://doi.org/10.1007/978-1-4939-0354-2_7.

37. Hall, T., Biosciences, I., and Carlsbad, C. (2011). BioEdit: an important software for molecular biology. GERF Bull. Biosci. *2*, 60–61.

38. Sambrook, J., Fritsch, E.F., and Maniatis, T. (1989). Molecular Cloning: A Laboratory Manual.

39. Van Driel, T.B., Nelson, S., Armenta, R., Blaj, G., Boo, S., Boutet, S., Doering, D., Dragone, A., Hart, P., Haller, G., et al. (2020). The ePix10k 2-megapixel hard X-ray detector at LCLS. J. Synchrotron Radiat. *27*, 608–615. https://doi.org/10.1107/S1600577520004257.

40. Blaj, G., Dragone, A., Kenney, C., Abu-Nimeh, F., Caragiulo, P., Doering, D., Kwiatkowski, M., Markovic, B., Pines, J., and Weaver, M. (2019). Performance of ePix10K, a High Dynamic Range, Gain Auto-Ranging Pixel Detector for FELs*1* (AIP Publishing LLC), 060062. https://doi.org/10.1063/1.5084693.

41. Nazari, R., Zaare, S., Alvarez, R.C., Karpos, K., Engelman, T., Madsen, C., Nelson, G., Spence, J.C.H., Weierstall, U., Adrian, R.J., and Kirian, R.A. (2020). 3D printing of gas-dynamic virtual nozzles and optical characterization of high-speed microjets. Opt Express *28*, 21749–21765. https://doi.org/10.1364/OE.390131.

42. DePonte, D.P., Weierstall, U., Schmidt, K., Warner, J., Starodub, D., Spence, J.C.H., and Doak, R.B. (2008). Gas dynamic virtual nozzle for generation of microscopic droplet streams. J. Phys. D Appl. Phys. *41*, 195505. https://doi.org/10.1088/0022-3727/41/19/195505.

43. Doppler, D., Rabbani, M.T., Letrun, R., Cruz Villarreal, J., Kim, D.H., Gandhi, S., Egatz-Gomez, A., Sonker, M., Chen, J., Koua, F.H.M., et al. (2022). Co-flow injection for serial crystallography at X-ray free-electron lasers. J. Appl. Crystallogr. *55*, 1–13. https://doi.org/10.1107/S1600576721011079.

44. Sonker, M., Doppler, D., Egatz-Gomez, A., Zaare, S., Rabbani, M.T., Manna, A., Villarreal, J.C., Nelson, G., Ketawala, G.K., and Karpos, K. (2022). Capillary coupled electrically stimulated segmented flow generators for reduced sample consumption in serial femtosecond crystallography. Biophys. Rep. 100081. https://doi.org/10.1016/j.bpr.2022.100081.

45. Sierra, R.G. (2016). The Microfluidic Electrokinetic Sample Holder for Serial Femtosecond X-Ray Crystallography (Stanford University).

46. Kabsch, W. (2010). Xds. Acta Crystallogr. D Biol. Crystallogr. *66*, 125–132.

47. Mariani, V., Morgan, A., Yoon, C.H., Lane, T.J., White, T.A., O'Grady, C., Kuhn, M., Aplin, S., Koglin, J., Barty, A., and Chapman, H.N. (2016). OnDA: online data analysis and feedback for serial X-ray imaging. J. Appl. Crystallogr. *49*, 1073–1080. https://doi.org/10.1107/S1600576716007469.

48. Barty, A., Kirian, R.A., Maia, F.R.N.C., Hantke, M., Yoon, C.H., White, T.A., and Chapman, H. (2014). Cheetah: software for high-throughput reduction and analysis of serial femtosecond X-ray diffraction data. J. Appl. Crystallogr. *47*, 1118–1131. https://doi.org/10.1107/S1600576714007626.

49. White, T.A., Kirian, R.A., Martin, A.V., Aquila, A., Nass, K., Barty, A., and Chapman, H.N. (2012). CrystFEL: a software suite for snapshot serial crystallography. J. Appl. Crystallogr. *45*, 335–341. https://doi.org/10.1107/S0021889812002312.

50. White, T., Kirian, R., Beyerlein, K., Aquila, A., Martin, A., Galli, L., et al. (2020). CrystFEL-Release Notes for Version 0.9. 0. https://www.desy.de/~twhite/crystfel/changes.html.

51. Gevorkov, Y., Yefanov, O., Barty, A., White, T.A., Mariani, V., Brehm, W., Tolstikova, A., Grigat, R.-R., and Chapman, H.N. (2019). XGANDALF–extended gradient descent algorithm for lattice finding. Acta Crystallogr. A Found. Adv. *75*, 694–704.

52. Duisenberg, A.J.M. (1992). Indexing in single-crystal diffractometry with an obstinate list of reflections. J. Appl. Crystallogr. *25*, 92–96. https://doi.org/10.1107/S0021889891010634.

53. Powell, H.R., Johnson, O., and Leslie, A.G.W. (2013). Autoindexing diffraction images with iMosflm. Acta Crystallogr. D Biol. Crystallogr. *69*, 1195–1203.

54. Brehm, W., and Diederichs, K. (2014). Breaking the indexing ambiguity in serial crystallography. Acta Crystallogr. D Biol. Crystallogr. *70*, 101–109. https://doi.org/10.1107/S1399004713025431.

55. Winn, M.D., Ballard, C.C., Cowtan, K.D., Dodson, E.J., Emsley, P., Evans, P.R., Keegan, R.M., Krissinel, E.B., Leslie, A.G.W., McCoy, A., et al. (2011). Overview of the CCP4 suite and current developments. Acta Crystallogr. D Biol. Crystallogr. *67*, 235–242.

56. Evans, P.R., and Murshudov, G.N. (2013). How good are my data and what is the resolution? Acta Crystallogr. D Biol. Crystallogr. *69*, 1204–1214. https://doi.org/10.1107/S0907444913000061.

57. Murshudov, G.N., Skubák, P., Lebedev, A.A., Pannu, N.S., Steiner, R.A., Nicholls, R.A., Winn, M.D., Long, F., and Vagin, A.A. (2011). REFMAC5 for the refinement of macromolecular crystal structures. Acta Crystallogr. D Biol. Crystallogr. *67*, 355–367. https://doi.org/10.1107/S0907444911001314.

58. Emsley, P., Lohkamp, B., Scott, W.G., and Cowtan, K. (2010). Features and development of coot. Acta Crystallogr. D Biol. Crystallogr. *66*, 486–501. https://doi.org/10.1107/S0907444910007493.

59. Liebschner, D., Afonine, P.V., Moriarty, N.W., Poon, B.K., Sobolev, O.V., Terwilliger, T.C., and Adams, P.D. (2017). Polder maps: improving OMIT maps by excluding bulk solvent. Acta Crystallogr. D Struct. Biol. *73*, 148–157. https://doi.org/10.1107/S2059798316018210.

60. Joosten, R.P., Long, F., Murshudov, G.N., and Perrakis, A. (2014). The PDB_REDO server for macromolecular structure model optimization. IUCrJ *1*, 213–220. https://doi.org/10.1107/S2052252514009324.

61. The PyMOL Molecular Graphics System, Version 2.0 (2022). (Schrodinger, LLC).

62. Juers, D.H., and Ruffin, J. (2014). MAP_CHANNELS: a computation tool to aid in the visualization and characterization of solvent channels in macromolecular crystals. J. Appl. Crystallogr. *47*, 2105–2108. https://doi.org/10.1107/S160057671402281X.

63. Laskowski, R.A., and Swindells, M.B. (2011). LigPlot+: multiple ligand–protein interaction diagrams for drug discovery. J. Chem. Inf. Model. *51*, 2778–2786. https://doi.org/10.1021/ci200227u.

STAR★METHODS

KEY RESOURCES TABLE

REAGENT or RESOURCE	SOURCE	IDENTIFIER
Antibodies		
Penta-His mouse monoclonal IgG	Qiagen	Cat#34660
IRDye® 800CW goat anti-mouse IgG Secondary antibody	LI-COR biosciences	Cat#926–32210
Bacterial and virus strains		
E. coli BL21-Gold(DE3)	Agilent Technologies	Cat#230124
Chemicals, peptides, and recombinant proteins		
S.O.C. Medium	ThermoFisher	Cat#15544034
Yeast Extract	Thomas Scientific	Cat#1037530500
Tryptone	MilliporeSigma	Cat#61044-5KG
Sodium Chloride	MilliporeSigma	Cat#S9888-1KG
Potassium phosphate dibasic	MilliporeSigma	Cat#P3786-1KG
Carbenicillin disodium	Goldbio	Cat#C-103-25
D-(+)-glucose	Sigma	Cat#G5767-500G
Isopropyl β- d-1-thiogalactopyranoside (IPTG)	MilliporeSigma	Cat#420322–25G
4-(2-hydroxyethyl)-1-piperazineethanesulfonic acid (HEPES)	Sigma	Cat#H3375-1KG
Imidazole	Sigma	Cat#I2399-500G
Tris(2-carboxyethyl) phosphine hydrochloride (TCEP-HCl)	Goldbio	Cat#TCEP1
InstantBlue Coomassie Protein Stain	Abcam	Cat#ab119211
Sodium Citrate Dihydrate	Fisher	Cat#BP327-1
(±)-2-methyl-2,4-pentanediol (MPD)	Sigma	Cat#M9671-50G
50% w/v Polyethylene glycol 2,000	Hampton Research	Cat#HR2-592
50% w/v Polyethylene glycol 1,000	Hampton Research	Cat#HR2-523
Tris Base	Gojira Fine Chemicals, LLC	Cat#TR1003
Boric acid	Alfa Aesar	Cat#12680
40% Acrylamide/Bis (19:1)	Bio-Rad	Cat#1610144
10X DTT (100 mM)	NEB	Cat#B1034A
KCl	EMD Millipore	Cat#PX1405-1
$MnCl_2$	Sigma	Cat#M3634
Urea	Gojira Fine Chemicals, LLC	Cat#UU1001
EDTA	Thermo Scientific	Cat#17892
Ammonium persulfate	Acros organics	Cat#327081000
TEMED	Bio-rad	Cat#161–0801
Bromophenol Blue	MilliporeSigma	Cat#114391-5G
Xylene cyanol	MilliporeSigma	Cat#X4126-10G
Critical commercial assays		
BioRad Protein assay dye reagent concentrate	Bio-Rad	Cat#5000006
Deposited data		
Room temperature structure of NSP15 Endoribonuclease from SARS-CoV-2 solved using SFX	This paper	PDB: 7K9P
Plasmid: pHis-TEV-Nsp15	This paper	GenBank: ON191567
Oligonucleotides		
3′ IRDye® 800CW labeled RNA oligonucleotides	Integrated DNA Technologies (IDT)	N/A

(*Continued on next page*)

Continued

REAGENT or RESOURCE	SOURCE	IDENTIFIER
Recombinant DNA		
Plasmid: pHis-TEV-Nsp15	Genscript	N/A
Software and algorithms		
OnDA	(Mariani et al., 2016)[47]	https://github.com/omdevteam/om
Hybrid: Cheetah & OnDA (unpublished)	(Barty et al., 2014)[48] (Mariani et al., 2016)[47] developed by Alexandra Tolstikova at CFEL (DESY, Hamburg) (unpublished)	https://github.com/omdevteam/om
CrystFEL version 0.9.1	(White et al., 2012[49]; White et al., 2020[50])	https://www.desy.de/~twhite/crystfel/
xgandalf	(Gevorkov et al., 2019)[51]	N/A
DirAX	(Duisenberg, 1992)[52]	http://www.crystal.chem.uu.nl/distr/dirax/
Mosflm	(Powell et al., 2013)[53]	N/A
XDS	(Kabsch, 2010)[46]	https://xds.mr.mpg.de
AMBIGATOR (CrystFEL package)	(Brehm and Diederichs, 2014)[54]	https://www.desy.de/~twhite/crystfel/
CCP4	(Winn et al., 2011)[55]	http://www.ccp4.ac.uk/
XSCALE	(Kabsch, 2010)[46]	https://xds.mr.mpg.de
AIMLESS	(Evans and Murshudov, 2013)[56]	http://www.ccp4.ac.uk/
REFMAC5	(Murshudov et al., 2011)[57]	http://www.ccp4.ac.uk/
COOT	(Emsley et al., 2010)[58]	http://www2.mrc-lmb.cam.ac.uk/Personal/pemsley/coot/
Phenix	(Liebschner et al., 2017)[59]	http://www.phenix-online.org/
PDB-redo	(Joosten et al., 2014)[60]	https://pdb-redo.eu
PyMOL Molecular Graphics System	(Schrödinger, LLC)	http://pymol.org/
MAP_CHANNELS v.0.5.	(Juers and Ruffin, 2014)[62]	http://people.whitman.edu/~juersdh/Channel_Mapping.shtm
LigPlot + v.2.2	(Laskowski and Swindells, 2011)[63]	https://www.ebi.ac.uk/thornton-srv/software/LIGPLOT/
Other		
HisTrap HP, 5mL	GE Healthcare	17-5248-02
NuPAGE 4–12% Bis-Tris, 1.0 mm mini protein gel, 17 well	Fisher	NP0329BOX

RESOURCE AVAILABILITY

Lead contact

For further information and requests regarding reagents, please contact Petra Fromme (pfromme@asu.edu).

Materials availability

The plasmid generated in this project was deposited in GenBank with the accession number listed in this manuscript.

Data and code availability

The room temperature Nsp15 structure was deposited in the Protein Data Bank under accession code PDB: 7K9P.

This paper does not report any original code. Any additional information required to reanalyze the data reported in this paper is available from the lead contact upon request.

EXPERIMENTAL MODEL AND SUBJECT DETAILS

For protein expression, competent *E. coli* BL21-gold (DE3) cells were purchased from Agilent Technologies. Cells transformed with the pHis-TEV-Nsp15 plasmid were cultured in LB Lennox media by inoculating a stater culture (100 mL) with a single colony or 1% (v/v) of the starter culture to a 1 L culture. Cultures were grown at 37°C with 180 rpm shaking, unless specified otherwise for protein induction.

METHOD DETAILS

Vector design and cloning

The expression plasmid harboring the DNA sequence for the NendoU protein, pHis-TEV-Nsp15, was designed based on the protein sequence information reported by Kim and co-workers.[7] The plasmid pHis-TEV-Nsp15 expresses a protein sequence identical to that in PDB 6VWW [7] and was purchased from GenScript. The parent vector, pET-11b, confers ampicillin resistance, uses the T7*lac* promoter and T7 terminator, contains the *lacI* gene and has a ColE1 replication origin. The DNA sequence of Nsp15-TEV-His_6 was optimized for expression in *E. coli* using GenScript's OptimumGene algorithm (Figure S7). Figure S8 contains an alternate plasmid design and supporting expression.The complete DNA sequence, and expressed protein sequence can be found in Tables S1 and S2, respectively.

In vivo expression of NendoU protein

Expression of the wildtype NendoU was optimized from methodology reported previously.[7,36] The plasmid for Nsp15-TEV-His_6 was obtained from GenScript and transformed into competent *E. coli* cells (BL21-Gold (DE3) strain, Agilent Technologies). Transformation was performed by adding 20 ng of plasmid to 100 μL of competent cells and incubating on ice for 30 minutes. Cells were then heat shocked at 42 °C for 45 seconds and then rested on ice for two minutes. Super Optimal broth with Catabolite repression (SOC) was added to the cells for a total volume of 1 mL and grown at 37°C for one hour with agitation at 250 rpm. Cells were then plated onto Luria broth (LB) agar plates supplemented with 50 μg/mL carbenicillin and grown overnight at 37°C. The following day, starter cultures were prepared by inoculation of a single colony into a 50 mL LB Lennox media supplemented with 50 μg/mL carbenicillin and grown at 37°C overnight with continuous agitation at 180 rpm. Large cell cultures of 1 L were inoculated with 1% (v/v) of starter culture and grown at 37°C with continuous agitation at 180 rpm until the optical density at 600 nm (OD_{600}) reached values of ~1.0. Cultures were then induced with 0.2 mM IPTG, 0.1% glucose, and 40 mM of potassium phosphate dibasic, transferred to an incubator at 18°C for 18-hours of growth with continuous agitation at 180 rpm. Whole cells were analyzed by SDS-PAGE gel with InstantBlue Coomassie stain and anti-His Western blot. Cells were harvested by centrifugation at 7,500 × g for 15 minutes at 4°C and stored at −80°C.

Development of an *in vitro* expression system for NendoU protein

Initial screening was performed by running 50 μL of cell-free reactions using an Invitrogen Expressway Kit for 4 hours with 0.5–2 μg of pHis-TEV-Nsp15 plasmid and 2 μg of Green Fluorescent Protein (GFP) as the control, incorporating 1 μL of Fluorotect reagent into each reaction. Lysates were denatured and run under reducing conditions on 4–12% BIS-TRIS SDS-PAGE gels and imaged at 600 nm and 700 nm using a LI-COR Odyssey Fc Imaging system (Figure 1A). Expression scale-up and purification were carried out in 1 mL reaction tubes using the Rabbit Biotech RTS 500 ProteoMaster *E. coli* HY Kit for protein expression. Briefly, lyophilized reaction components (*E. coli* lysate, reaction mixture, amino acid mixture, and methionine) were dissolved in reconstitution buffer and combined as specified by the manufacturer. A total of 20 μg of pHis-TEV-Nsp15 plasmid were added to the lysate mixture and the reactions were incubated at 37°C for 5 hours. Small-scale purification of the cell free lysates were performed as follows. Gravity-flow immobilized nickel affinity chromatography was used to purify the protein using 50 mM sodium phosphate pH 8, 150 mM NaCl as the equilibration buffer (EB) at 4°C. Expression products were incubated and bound to the Ni column for 1 hour in EB containing 5 mM imidazole, washed with six column volumes (CVs) of EB containing 10 mM imidazole, and subsequently eluted with 1.8 CVs containing 250 mM imidazole, followed by 0.3 CVs containing 500 mM imidazole. Eluted fractions were verified for protein purity with SDS-PAGE (Figure 1B). The protein concentration was measured using a Q-bit protein assay and fluorimeter from Molecular Probes. Eluted fractions E2-E5 containing NendoU were combined, dialyzed into 20 mM HEPES-Na pH 7.5, 150 mM NaCl, 1 mM TCEP-HCl, and concentrated to 5 mg/mL with 10 kDa molecular weight cut-off (MWCO) spin filtration concentrators. The protein was further purified with a Superdex 200 10/300 increase GL column using the buffer 20 mM HEPES-Na, pH 7.5, 150 mM NaCl, 1 mM TCEP (Figure 1C).

Large scale protein purification of NendoU

The purification protocol used was based on Kim et al., 2020 with modifications.[7] The protein from this large scale purification was used for subsequent crystallization and activity assay experiments. Briefly, cell pellets were resuspended in 10% (w/v) lysis buffer (50 mM HEPES-Na, pH 8.0, 500 mM NaCl, 20 mM imidazole) and lysed by sonication (2 sec ON / 2 sec OFF for 2 minutes for five cycles with 2 minutes rest on ice). The lysate was centrifuged at 45,000 × g for 30 minutes. Supernatant containing NendoU protein was loaded onto a Ni-NTA chromatography column (GE Health Care HisTrap™ HP, 5mL) and purification was performed using an ÄKTA Pure FPLC at 4 °C. After collecting the flow through, the column was washed with 20 CVs of buffer 50 mM HEPES-Na, pH 7.5, 500 mM NaCl containing 20 mM imidazole followed by a wash with 20 CVs of the same buffer but an increased imidazole concentration of 500 mM (Figures S1A and S1B). The eluted protein was concentrated with a spin concentrator (Amicon Ultra-0.5 mL centrifugal filters; 30 kDa MWCO) to a volume of 0.5 mL and further purified by size exclusion chromatography (SEC) using a Superdex 200 10/300 increase GL column equilibrated in 20 mM HEPES-Na, pH 7.5, 150 mM NaCl, 1 mM TCEP and run at 0.5 mL/min (Figure S1C). The NendoU hexamer eluate (11–12 mL) was analyzed by SDS-PAGE gel with InstantBlue Coomassie stain and anti-His Western blot (Figures S1D and S1F). The protein was concentrated to 10 mg/mL for storage in −80°C until future use. Dynamic Light Scattering (DLS) was performed using a SpectroSize 302 spectrometer from Molecular Dimensions with the

corresponding software for data collection and processing (Figure S1E). Samples were analyzed at ambient temperature at concentrations between 1 and 15 mg/mL in SEC buffer.

Crystallization of NendoU protein

NendoU microcrystals were obtained using two approaches: crystallization by concentration at low ionic strength and batch with agitation. For crystallization by concentration, purified protein (in 20 mM HEPES-Na, pH 7.5, 150 mM NaCl, 1 mM TCEP) was concentrated (Amicon Ultra-0.5 mL centrifugal filters; 30 kDa MWCO) to 60–80 mg/mL at 7,000 × g, 12°C in 10-minute runs and resuspended with a 200 μL pipette between steps to reduce settling of the protein onto the membrane. At concentrations above 60 mg/mL, the concentrated protein appeared turbid. At this point, the sample was transferred to a microcentrifuge tube and resuspended in its buffer with a pipette to increase turbidity and the crystal suspension was stored at 4°C to mature overnight. Crystal formation was verified under an optical microscope. A schematic of the overall set-up and schematic phase diagram can be seen in Figure 3A.

For crystals grown by batch with agitation in the presence of sodium citrate, purified NendoU protein was concentrated to 40 mg/mL using the same procedure as for crystallization by concentration. The precipitant (300 μL) composed of 0.1 M sodium citrate, pH 5.6, 10% MPD, 10% PEG 2000 was placed on the bottom of a glass vial (7 mL vial, screw top, clear glass, from Millipore Sigma catalog #27151), which in turn was placed on a magnetic stir plate at room temperature with a micro-stir bar gently spinning at ~200 rpm. Next, the protein (50 μL) was added dropwise at 1 drop per second to the precipitant while gently stirring. A schematic of the overall set-up can be seen in Figure 3B. The mixture turned turbid during addition, and the crystal suspension was incubated for 24 hours at ambient temperature.

Batch crystallization condition were optimized to omit citrate in the precipitant. Protein (50 μL of a 40 mg/mL solution) was placed on the bottom of a 1.5 mL reaction tube. Batch crystallization was performed by rapidly mixing the protein with precipitant for a total of one part protein to six parts precipitant solution, corresponding to reaction volumes of 50 μL and 300 μL respectively per experiment; the precipitant volume was added to the protein solution over twelve intervals of 25 μL aliquots with rapid mixing and 15 seconds incubation between additions. Two precipitant conditions were identified: [0.2 M Calcium Acetate, 0.1M HEPES pH 7.5, 10%(w/v) PEG 8000] or [0.2 M NaCl, 0.1M Sodium Potassium Phosphate, 10%(w/v) PEG 8000] based on Kim et al.[11] The crystallization solutions were incubated at 4°C overnight. Crystallization experiments of NendoU were visualized by optical microscopy with a polarizing filter by sandwiching a 2 μL sample droplet between two coverslips (Figure 3).

RNA substrate design and functional assays

Multiple sequence alignment was performed manually using the BioEdit program.[37] RNase-free conditions were maintained throughout the experiments as follows. IRdye 800CW near infra-red dye labeled oligonucleotides were commercially synthesized with RNase-free HPLC purification (Integrated DNA Technologies) and resuspended in milliQ water. Aliquots of stock solutions were stored at −80°C until further use. Labeled RNA oligonucleotide-containing reactions were handled using RNase-free consumables and standard practices were followed to avoid RNase contamination.[38] These practices were applied in the handling of purified NendoU protein and in related crystallization experiments for stock solutions, buffers, and equipment (ex., pipettes, tube racks) in RNase-free areas to avoid contamination. RNase Zap solution was used to clean equipment used for handling and preparing the samples along with gloves prior to RNase-free work.

In solution endoribonuclease assays were performed as follows. Purified NendoU protein was diluted to a final concentration of 6 μM protein in 1× assay buffer (50 mM Tris-HCl pH 7.5, 50 mM KCl and 1 mM DTT). Lyophilized RNA oligos labeled at the 3′ end with IRDye 800CW near-infrared (NIR) fluorescent dyes (Integrated DNA Technologies) were dissolved in nuclease-free water to prepare a 100 μM stock solution and later diluted with nuclease-free water to the 5 mM working concentration. NendoU cleavage reactions were carried out in 10 μL of total volume by mixing 5 μL of 2 × assay buffer, 2 μL nuclease-free water, 1 μL of 6 μM NendoU enzyme, and 1 μL of 5 μM RNA probe. Reactions were incubated for 5 mins at 25°C, followed by the addition of either 1 μL of nuclease-free water or 1 μL of 50 mM $MnCl_2$ and incubated for an additional 3 mins. Reactions were stopped by adding equal volumes of 2 × urea loading dye (8 M urea, 20 mM Tris-HCl pH 7.5, 1 mM EDTA, 0.05% (w/v) Xylene cyanol and 0.05% (w/v) Bromophenol blue), followed by incubation at 95°C for 2 mins and cooling on ice. One-tenth of the reactions were resolved on a 10% urea-PAGE gel or 15% urea-PAGE gel for short RNA substrates. Following electrophoresis, gels were scanned directly on a Typhoon NIR-IP scanner.

In crystal endoribonuclease assays were performed as follows. A microcrystal suspension of 1 μL (equivalent to ~16 nanomoles of NendoU protein) was incubated with 4.4 μL of crystallization buffer (0.1 M sodium citrate pH 5.5, 10% MPD, 20% PEG 1000) and 3.6 μL of 100 μM RNA substrate. The reaction was set up in duplicates. A separate reaction mixture without the RNA but with 3.6 μL of crystallization buffer was used as the negative control. All three reaction mixtures were incubated at 22°C for 30 mins. Then, 1 μL of 50 mM $MnCl_2$ was added to each of the reaction mixtures containing the RNA substrate and 1 μL of crystallization buffer was added to each mixture (duplicates and the control). The reaction mixtures were further incubated for 1 min. Then, 1 μL of reaction mixture was added to 19 μL of 2 × urea loading dye followed by incubation at 95°C for 2 mins and placed on ice until loading. Crystals from the rest of the reaction mixture were further allowed to settle and checked for birefringence under an optical microscope with a polarization filter. After imaging, the crystal suspension was centrifuged at 500 × g for 2 min at 4°C and 5 μL of the supernatant was used for a Bradford assay according to manufacturer's instructions (BioRad protein assay – cuvette format, Figure 4).

X-ray diffraction data collection and analysis

Serial fs crystallography (SFX) diffraction images were recorded at the Macromolecular Femtosecond Crystallography (MFX) beamline of the LCLS at SLAC. Data were collected at 120 Hz repetition rate at an energy of 9.79 keV with 30 fs pulse duration and an average flux of 0.3–0.5 mJ/pulse. X-ray diffraction data were collected on the ePix10k detector[39,40] in the adaptive gain switching mode in the low/medium gain setting.

Two established SFX injection methods were explored for delivering the crystals into the X-ray interaction region. The first was a standard gas dynamic virtual nozzle (GDVN) liquid injection set-up,[41,42] for which the sample was delivered through a 3D-printed nozzle with a 75 μm inner diameter sample line into the chamber that had been purged with helium (sample flow rate of 25 μL/min and a helium sheath gas pressure of 300 psi). The 3D-printed GDVNs were fabricated with a Photonics GT (Nanoscribe GmbH, Germany) high resolution printer using proprietary photoresist IP-S (Nanoscribe GmbH, Germany). The nozzles were otherwise printed and assembled as describes previously.[41,43,44]

Alternatively, the crystals were injected using the electro-spinning jet produced by the microfluidic electrokinetic sample holder (MESH) injector[45] operated in ambient conditions (sample flow rate of 3–5 μL/min). All crystal samples were filtered through 30 μm mesh filters before sample delivery and loaded into 1.5 mL stainless steel reservoirs where they were gently rotated using an anti-settling device to prevent settling.

The online hit rate and background correction for the live display were performed using ''OM'', a customized version of OnDa[46,47] for LCLS. Off-line calibration and hit finding were performed with a new hybrid version of Cheetah[48] and OnDA[47] developed by Alexandra Tolstikova at CFEL (DESY, Hamburg) (unpublished). Peak finding was performed using the *peakfinder 8* algorithm with the following parameters: adc_threshold = 500, minimum_SNR = 5.0, min_pixel_count = 1, local_bg_radius = 4, min_res = 80, max_res = 450. Diffraction patterns with more than 12 peaks were classified as hits. The hits, along with the recorded peak positions, were indexed with the software CrystFEL version 0.9.1.[49,50] Successive indexing attempt were made employing XGANDALF,[51] DirAX,[52] MOSFLM,[53] and XDS[46] in this order. Due to the indexing ambiguity for serially collected ''still'' diffraction patterns in point group P63, the list of indexed diffraction intensities was consequently passed through the program AMBIGATOR[54] (CrystFEL package) applying the re-indexing operator *-h-k,k,-l*. The reflection intensities were then merged and integrated using PARTIALATOR (CrystFEL package) applying 3 iterations and the unity model.

The merged reflection intensities were converted to CCP4 compatible *mtz* format[55] using XSCALE,[46] where they were then scaled using the AIMLESS program.[56] Phasing was performed by molecular replacement using the crystal structure of NendoU PDB entry 6XDH as the search model (Dranow et al., unpublished results) with all solvent and ligand atoms removed. The structure was refined applying alternate cycles of REFMAC5[57] and manual refinement performed with COOT.[58] Ultimately, citrate (and water) molecules were fitted and refined into the electron density in the active site and POLDER maps were calculated in Phenix.[59] The final model was passed through the web interface PDB-redo[60] for a final cycle of refinement prior to submission.

Figures were prepared using PYMOL (Schrödinger, LLC).[61] Channel sizes and maps through the crystal were calculated using MAP_CHANNELS v.0.5,[62] and ligand plots were produced with LigPlot + v.2.2.[63]

QUANTIFICATION AND STATISTICAL ANALYSIS

Data statistics for X-ray crystallographic structure determination are shown in Table 1.